Opto-Electronic Advances

Review

2022, Vol. 5, No. 10

DOI: 10.29026/oea.2022.210058

A review and a statistical analysis of porosity in metals additively manufactured by laser powder bed fusion

Dawei Wang[1,5], Huili Han[2], Bo Sa[1], Kelin Li[1], Jujie Yan[1], Jiazhen Zhang[3], Jianguang Liu[3], Zhengdi He[4], Ning Wang[4]* and Ming Yan[1,5]*

Additive manufacturing (AM), or 3D printing, is an emerging technology that "adds" materials up and constructs products through a layer-by-layer procedure. Laser powder bed fusion (LPBF) is a powder-bed-based AM technology that can fabricate a large variety of metallic materials with excellent quality and accuracy. However, various defects such as porosity, cracks, and incursions can be generated during the printing process. As the most universal and a near-inevitable defect, porosity plays a substantial role in determining the mechanical performance of as-printed products. This work presents a comprehensive review of literatures that focused on the porosity in LPBF printed metals. The formation mechanisms, evaluation methods, effects on mechanical performance with corresponding models, and controlling methods of porosity have been illustrated and discussed in-depth. Achievements in four representative metals, namely Ti−6Al−4V, 316L, Inconel 718, and AlSi10Mg, have been critically reviewed with a statistical analysis on the correlation between porosity fraction and tensile properties. Ductility has been determined as the most sensitive property to porosity among several key tensile properties. This review also provides potential directions and opportunities to address the current porosity-related challenges.

Keywords: additive manufacturing; laser powder bed fusion; selective laser melting; porosity; defects; mechanical performance; metallic materials; perspectives

Wang DW, Han HL, Sa B, Li KL, Yan JJ et al. A review and a statistical analysis of porosity in metals additively manufactured by laser powder bed fusion. *Opto-Electron Adv* **5**, 210058 (2022).

Introduction

Overview of additive manufacturing of metals

Additive manufacturing (AM), or 3D printing, is a rising star in the field of manufacturing technology. AM technologies are renowned for lifting the geometric constraints of design and fabricating products directly from digital models[1−3]. Materials are "added" up during AM processing, making it the distinguishing feature that opposed to traditional subtractive and formative manufacturing. According to the literatures[4−8] and the classifications proposed by the American Society for Testing and Materials (ASTM)[9], plentiful materials including metals,

[1]Department of Materials Science and Engineering, and Shenzhen Key Laboratory for Additive Manufacturing of High Performance Materials, Southern University of Science and Technology, Shenzhen 518055, China; [2]Department of Mechanical and Energy Engineering, Southern University of Science and Technology, Shenzhen 518055, China; [3]COMAC Beijing Aircraft Technology Research Institute, Beijing 102211, China; [4]Shenzhen Technology University, Shenzhen 518118, China; [5]Jiaxing Research Institute, Southern University of Science and Technology, Jiaxing 314031, China.

*Correspondence: N Wang, E-mail: wangning@sztu.edu.cn; M Yan, E-mail: yanm@sustech.edu.cn

Received: 7 May 2021; Accepted: 12 July 2021; Published online: 25 July 2022

intermetallics, polymers[10], ceramics, and composites, can be additively manufactured. The application of AM significantly reduces the time consumption and economic cost of prototyping and mold making[11,12]. Scientific researches and technological developments can be substantially facilitated through utilizing the AM technologies wisely.

The AM of metals has been attracting intense research and industrial interest recently[13–15]. As-printed metal components have been vastly used in healthcare, aerospace, automotive, and marine industries[16,17]. Most commercially-available AM technologies use metal powders or wires as the feedstock[11]. Feedstock materials are melted by heat sources, such as laser/electron beams and electric arc, then deposited to the products[14]. The motions of heat sources are numerically guided on the basis of sliced digital models. Thus, the products are constructed layer-by-layer to their final form. The powder-bed-based AM technologies are well adopted at present to fabricate metallic products with high accuracy and good quality[18–20]. A powder bed is paved on the building substrate and subsequently scanned by the heat source. A layer is therefore "printed" through the selective melting or sintering. The metals fabricated by powder-bed-based AM are able to archive excellent mechanical performance and high relative density (up to 99.9%)[8].

This review focuses on the laser powder bed fusion (LPBF) technology (also known as selective laser melting, SLM) that uses laser beam as the heat source. As a mainstream technology for the AM of metals[21,22], LPBF is chosen for its capability of shaping plentiful metals and its universality in both research and industrial applications[23]. The products are "printed" through a fully melting of feedstock powder and the subsequent solidification. A schematic illustration of LPBF processing is presented in Fig. 1.

Overview of LPBF processing and defects

The feedstock powder's morphology and granulometry can exert certain influences on the LPBF processing[24–26], whereas, the quality of as-printed metal products are generally controlled, even dictated by the processing parameters[8,27–31]. The laser power, scanning velocity, hatch spacing (spacing between scanning tracks), layer thickness, and scanning patterns are major parameters that can be adjusted to pursue a stable and defect-free melting-to-solidification process[16,23,32].

Appropriate laser parameters are required to maintain a stable molten pool, and to fuse the powder completely without activating detrimental instabilities[19,28]. However, the whole LPBF processing is a complicated operation. Melting at the beginnings, ends, and turns of scanning tracks is extremely difficult to stabilize due to the distinctive heating behaviors at those points[28]. The shadowing and related effects brought by laser spatter, vapor plume, and plasma are chaotic yet hard to measure[33–36]. Besides, the layer-by-layer deposition behavior of LPBF results in a cyclic heat history[37]. The accumulated impacts of heating/cooling cycles are difficult to evaluate. In summary, the instabilities and formation of defects in LPBF processing probably will not be entirely eliminated in the near future.

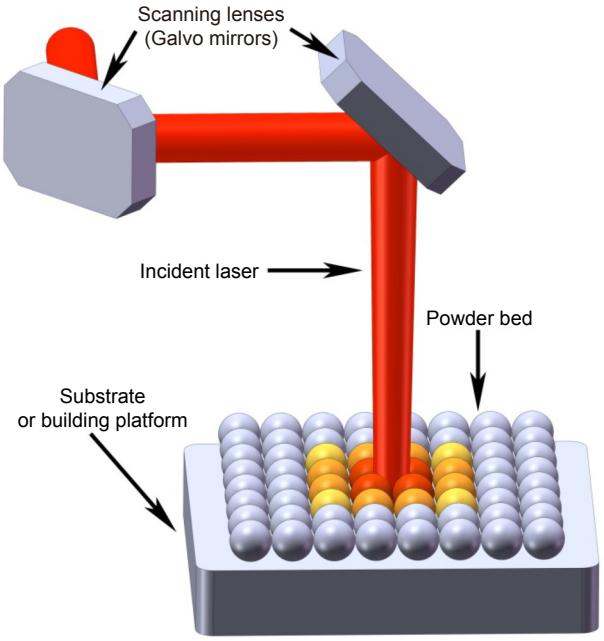

Fig. 1 | Schematic illustration of LPBF processing.

Defects are formed when printing deviates from its optimized range. Porosity, lack of fusion (LOF), unfavorable inclusion (e.g. unmelted particles), and cracks are common defects that observed in LPBF printed metal products[22,38,39]. Study of the defects and correlated mechanical effects is essential for the qualification and application of LPBF printed metal products[16,31].

Scope of this review

As-printed products containing fatal defects, such as large LOFs and cracks, are generally not acceptable for heavy loads or longtime services[40,41]. However, as a less detrimental but near-inevitable defect, porosity exists in almost every LPBF printed metal component. This review focuses on this most universal and difficult-to-eliminate defect. A thorough illustration of porosity

formation and evaluation is presented at first, followed by a collective analysis of its effects on mechanical performance. Ti–6Al–4V alloy, 316L stainless steel (SS), Inconel 718 superalloy, and AlSi10Mg alloy are selected as representative metals in the further analysis. Their uniaxial tensile properties are compiled with an in-depth discussion on the correlation between porosity and tensile properties. Furthermore, the controlling strategies of porosity as well as the current challenges and opportunities for LPBF applications have been summarized in the last part.

Formation mechanisms of the porosity in LPBF printed metals

Porosity existed in LPBF printed metals are classified into two main categories: the gas porosity and the LOF porosity[31,42,43]. Criteria of this classification is the morphological differences since gas porosity is generally spherical, whereas, LOF porosity is irregular and commonly has unmelted particles in it[30,44]. Representative observations of the two types of porosity are presented in Fig. 2. Both types of porosity are filled with inert shielding gas after LPBF processing. The entrapped gas prevents the total closure of pores even after hot isostatic pressing (HIP)[45,46]. What's worse, the porosity can even grow after heat treatments (HTs) due to the thermal expansion of entrapped gas[47,48].

Formation mechanisms of gas porosity

The gas porosity is induced by the entrapment of gas in the molten pool[31]. Both the melting depression and the cavities in feedstock powder can bring entrapped gas to the molten pool during LPBF processing[19,27,49,50]. The entrapped gas aggregates in the molten pool and forms spherical bubbles due to surface tension[51]. Bubbles that cannot escape before solidification become gas porosity in the as-printed products.

The vapor recoil pressure, surface tension, and Marangoni force (thermo-capillary force) are the three major forces that control the flow behavior in a molten pool[27,52,53]. On the basis of numerical simulations and experimental observations, recent studies[28,29] revealed that a stable molten pool can prevent the formation of porosity. On the contrary, if the balance of forces breaks, the resulted instabilities such as turbulence and keyholes have been observed to be responsible for the residual pores[54]. "Keyhole" is a description for the deep and narrow depression in the molten pool. Figure 3 displays the formation of pores through the collapse of keyhole tips. A high laser energy density boosts the recoil pressure thus increases the depth of depression[55]. Gas is therefore apt to be trapped in the deep keyholes. Furthermore, acoustic waves generated near the keyhole tips also facilitate the separation of tips[56], increasing the risk of forming gas porosity[50]. In summary, the keyhole melting mode is unfavorable from the perspective of porosity control when compared to the shallow and semicircular conduction melting mode.

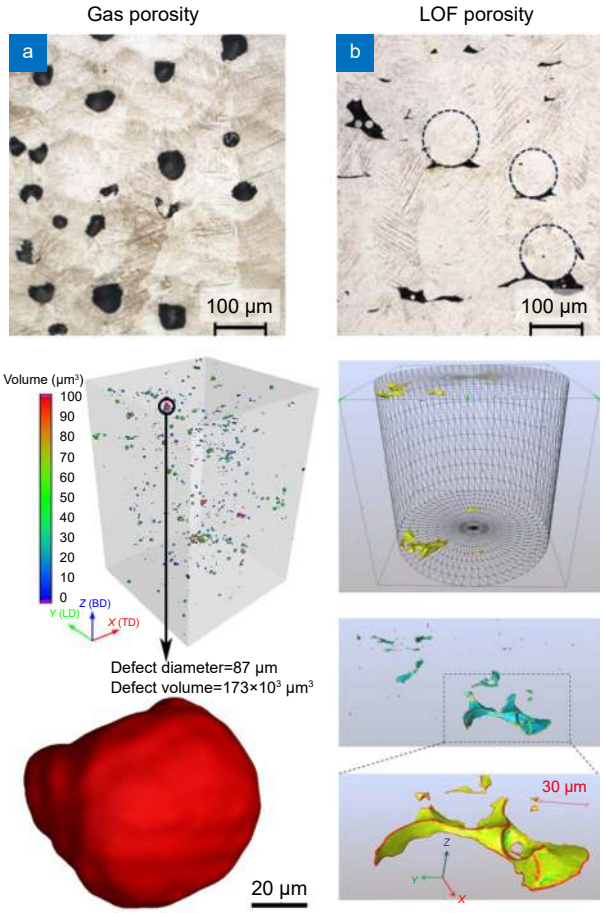

Fig. 2 | Representative cross-sections and 3D reconstructions of (**a**) gas porosity and (**b**) LOF porosity detected in LPBF printed metals. The dashed circles in (b) indicate unmelted feedstock powder. Figure reproduced with permission from (a) ref.[37,43], Elsevier; (b) ref.[43], Elsevier, under a Creative Commons Attribution-NonCommercial-NoDerivatives 4.0 International License.

The selective vaporization of volatile compounds and elements can provide additional recoil pressure and contribute to the chaos in molten pool[57–59]. This mechanism is capable of inducing massive porosity in as-printed metals and should be avoided[57,58]. However, such compounds and elements can be employed intentionally as foaming agents, to fabricate foam materials such as

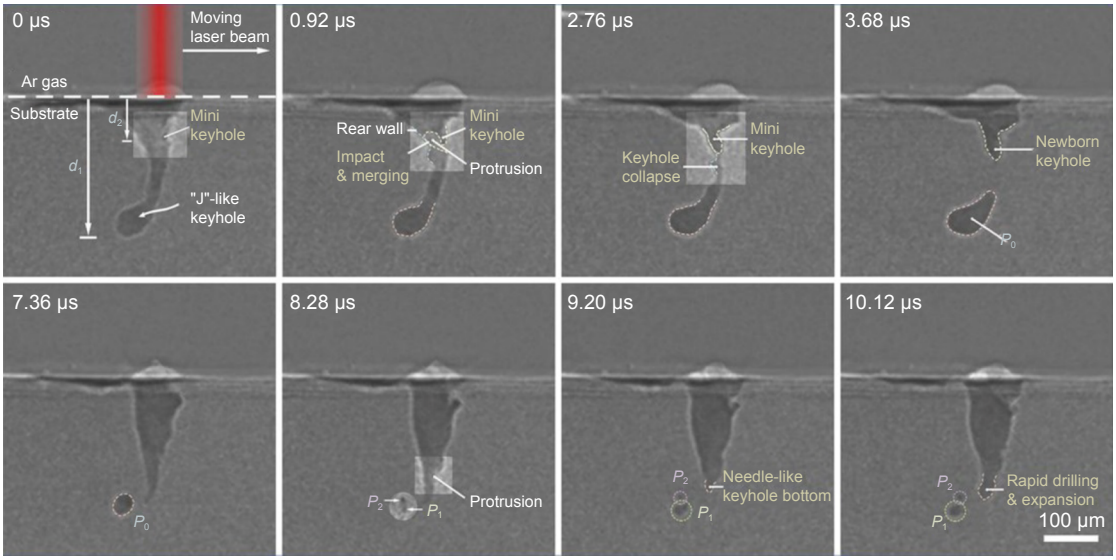

Fig. 3 | Synchrotron X-ray images of pores generated from keyholes. The time marks represent the delays of each graph after the first shot. Figure reproduced with permisson from ref.[29], The American Association for the Advancement of Science.

low-modulus implants and breathable mold steels[59]. In addition, the feedstock powders of LPBF, commonly prepared by gas atomization and plasma rotating electrode process, have intrinsic porosity[60–62]. The powder-entrapped porosity can be inherited if the feedstock powder was not completely melted[27,44]. Otherwise, the powder-entrapped gas releases during melting, which also increases the bubbles in molten pool and the risk of forming gas porosity[63]. Several studies reported the inherited porosity from powder in as-printed metals[64–66]. Wu et al.[64] confirmed a strong positive correlation between the porosity in feedstock powder and that in as-printed samples recently, through a comparative study using feedstock powders with different porosity fractions.

Formation mechanisms of LOF porosity

The LOF porosity is a result of local LOFs. When the laser energy is not enough to melt and fuse the material completely, separated surfaces will be generated and the voids among those surfaces become LOF porosity[31,43].

Origin of the LOF porosity can be divided into two categories: the incomplete melt of feedstock powder and the incomplete fusion of melting tracks. The first category of porosity can be eliminated through processing optimization[32], although it is still challenging if the feedstock powder contains refractory particles such as Mo and ceramics[67,68]. As mentioned before, the processing of LPBF is full of uncertainty. It is presently impractical to maintain the heat input stable for the whole scanning track[28]. Inhomogeneities in powder bed such as large voids and agglomeration, are still ubiquitous[24]. The spatter caused by unstable heat input and the powder agglomerations can produce significant shadowing effect, consuming the laser power and creating LOF voids in as-printed tracks[28,54]. Those large voids require longer time and more fluid to fill, making them may not be fully fused under regular processing parameters[69]. Even though the LOF porosity can be enclosed by the remelting when printing the layer above it[50], it is still a common defect in the as-printed refractory metals and metals that printed using irregular feedstock powders[68,70–72].

Measurement and evaluation of the porosity in LPBF printed metals

Measurement of the quantity, size, morphology, and spatial distribution of porosity is an initial step for evaluating LPBF printed metals. Measurement and evaluation methods presented in this review are divided into two classical categories: the destructive evaluation (DE) and the nondestructive evaluation (NDE). NDE methods do not permanently alter the inspected sample, making them feasible in both research and industrial applications[73,74]. On the other hand, DE methods also hold unique advantages such as the precise inspection of near-surface porosity[75]. Key descriptors and four mainstream methods of porosity evaluation are presented and analyzed briefly in the subsequent contents.

Descriptors of porosity

Measurement and statistical analysis of key characteristics are crucial for the study of porosity. The characteristics

of porosity in LPBF printed metals can be divided into four categories: quantity, size, morphology, and location[38,76–78]. The quantity of porosity is the most universal characteristic that appears in almost every piece of AM research works. Both volume-based (Archimedes, CT, etc.) and area-based (cross-sectional imaging, surface imaging, etc.) methods are able to provide the quantity data of porosity despite a variation in accuracy[76]. Meanwhile, the other three categories of key characteristics are dependent specifically on the imaging of porosity.

The size of porosity has been reported to have a strong effect on the void growth in plastic deformation[79,80]. The irregularity of porosity also increases with elevating size according to phenomenological statistics[37,81,82]. The square root of projected porosity area on a plane perpendicular to the maximum principal stress, $\sqrt{area}$, is broadly adopted to evaluate the scale effect of porosity[75,83–85]. According to the literatures on fracture mechanics, the largest pore holds the highest risk of inducing tensile and fatigue failures[41,86,87]. Statistical tools such as the extreme value statistics (EVS) have been employed to statistically estimate the size distribution of porosity, particularly the largest $\sqrt{area}$, to compensate the limited data sampling[88]. EVS method at 3D scale has shown success with the assistance of micro-CT in estimating the porosity size and fatigue life for LPBF printed AlSi10Mg alloy[81,85].

Porosity morphology is also critical for the evaluation since it is closely related to the stress concentration[89]. To avoid the exhausting calculation of curvatures at porosity interfaces, aspect ratio (AR) and sphericity (ψ) are used as two common descriptors in the studies of porosity morphology[84,90]. AR is used to measure the elongation of a pore, defined by[84]:

$$AR = \frac{L_{\text{minor}}}{L_{\text{major}}}, \tag{1}$$

where L_{minor} and L_{major} are lengths of minor and major axes, respectively. Sphericity is used to describe the geometric deviation of a pore from a sphere, defined by[90]:

$$\psi = 6V\sqrt{\frac{\pi}{A^3}}, \tag{2}$$

where V and A are volume and surface area of the pore, respectively. A visualized comparison of pores with different AR and sphericity is presented in Fig. 4. The two morphological descriptors can be easily calculated using data processing software then implemented in statistical analyses. Furthermore, 2D descriptors such as circularity and convexity are also valuable candidates for rating the porosity in LPBF printed metals[77].

The study on porosity clusters and spatial distribution of porosity in LPBF printed metals is currently at an early stage. Most quantitative researches are based on the artificial porosity that far dissimilar to the real situations[91–94]. It is promising to combine the actually-

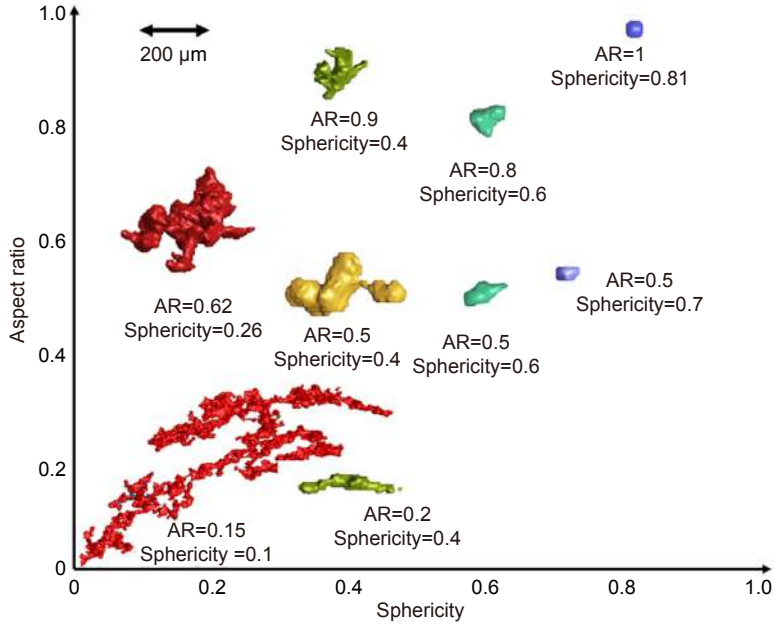

Fig. 4 | Porosity detected in LPBF printed Ti−6Al−4V alloy, with respective AR and sphericity values. Figure reproduced with permission from ref.[84], under a Creative Commons Attribution-NonCommercial-NoDerivatives 4.0 International License.

detected porosity with spatial statistics in the future analytical investigations, since a successful example has been established by Becker[80] for predicting the performance of powder metallurgy (PM) products.

The Archimedes method

The Archimedes method may be the oldest NDE approach to measure the density of solid samples with arbitrary shapes[95]. Samples are immersed in a liquid medium, such as water, to determine the margin of weight when weighed in air and in the liquid medium. Therefore, if the densities of liquid medium (ρ_m) and air (ρ_a) are known, the relative density of a sample is yielded as:

$$\rho_{rel} = \left\{ \left[\frac{(\rho_m - \rho_a)M_a}{M_a - M_m} + \rho_a \right] \Big/ \rho_{ref} \right\} \times 100\% , \quad (3)$$

where ρ_{rel} is relative density, M_a is mass weighed in air, M_m is mass weighed in the liquid medium, and ρ_{ref} is reference density of fully-dense material[78,96]. Although the Archimedes method only measures the whole quantity of porosity, it is still a practical and broadly-adopted method for evaluating the porosity in LPBF printed products[38,78,97,98]. A commercial Archimedes density meter usually uses small samples[78,99], but this approach can be smoothly expanded to large and heavy products through utilizing proper weighing instruments. The Archimedes method counts the contribution of all the internal voids, resulting in a higher detectivity of total porosity quantity compared to other imaging-dependent methods[37,97]. The Archimedes method has been extensively employed in the AM community to achieve a rapid overall evaluation of the as-printed products[74].

X-ray computed tomography

X-ray computed tomography (CT) is an advanced NDE technology that combines the X-ray imaging with the computed 3D reconstruction[100,101]. The intensity of X-ray attenuates after it transmitted a medium. The rate of attenuation varies among different mediums, e.g. the porosity and the dense metal. Therefore, the intensity of transmitted X-ray contains the inner structural information of the irradiated sample[100]. During CT inspection, the tested sample is exposed to X-ray radiation and a 2D slice is generated through collecting the X-ray intensity data from multiple angles with subsequent graphical reconstruction[39,78]. Those 2D slices are stacked and finally reconstructed into a 3D model with visible inner structure[100]. X-ray CT provides abundant information of the porosity in LPBF printed metals, including spatial distribution, morphology, dimensions and volumes, and other quantitative data[102]. Figure 5 demonstrates representative views of porosity distribution and a pore detected by CT.

X-ray CT method has received intense interest from the academia. Whereas, limitations of this method are hindering its application in certain circumstances. First, the resolution and efficiency of CT inspection are predominantly dependent on the dimensions of samples[100]. Metal samples need to be small, generally in millimeter scale, to ensure valid X-ray transmission and to achieve an ideal resolution[101]. Thus, small samples need to be cut out from large products before CT inspection, raising concerns on the damage caused by sampling and the generality of results[39,78]. Second, the X-ray CT method may not be able to detect all the micro pores or refined geometric features due to its nature[76,100]. Features smaller than several voxels cannot be reconstructed accurately due to the image artefacts[76]. The signal-to-noise ratio may become even worse at sample's surface and the edges of pores[100,103,104]. A comparison between the CT result and the actual cross-section of an LOF pore is

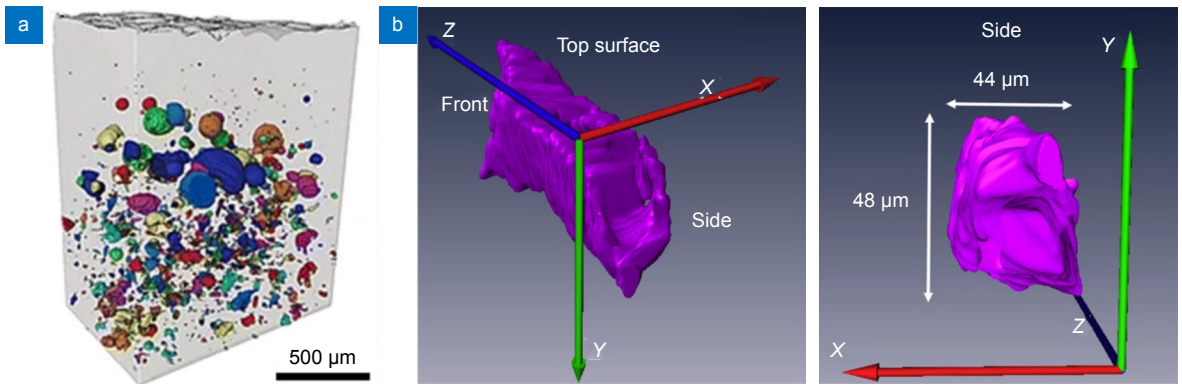

Fig. 5 | Representative 3D reconstructions of (**a**) the distribution of porosity in a Ti−6Al−4V sample and (**b**) views of a specific pore. Figure reproduced with permission from: (a) ref.[101], Springer Nature. (b) ref.[44], Elsevier.

presented in Fig. 6. The quanty of porosity calculated using CT is generally lower than that measured using the Archimedes method owing to the missed micro pores and edges[78,97].

2D imaging method

The 2D imaging method is a DE method on the basis of cross-section imaging. Samples are cut along specific planes, then polished and examined using microscopic instruments such as optical and scanning electron microscopes (SEM)[105]. This method provides the spatial distribution, morphology, and other characteristics of porosity similar to the CT method, but only in a 2D form. Several cross-sections will be prepared and examined to generate statistically-reliable results for a common sample[105,106]. Although the 2D imaging method destructs the sample and only provides 2D information, it is still favored because of the outstanding accessibility and detectivity[43,83,107,108]. A modern SEM is capable of producing graphs with nanometer-scale resolution[5]. The micro features of porosity can be captured clearly on the whole cross-section, which is evidently beneficial for the statistical study of geometric descriptors[83,105].

Ultrasonic method

Ultrasonic testing (UT) holds enormous applications in detecting defects in metal components[109–111]. This method is favored primarily for its excellent penetration depth in metals (can be as deep as several meters) and portability[73]. The inner defects are detected and evaluated through their interactions with the emitted ultrasonic waves[110]. Ultrasonic method has raised research interest in the community of AM recently[112–115]. Advanced ultrasonic technologies, such as laser ultrasonics and phased array ultrasonics, have been applied to pioneer the potential of UT in detecting porosity inside AM products[114,116]. Porosity-related time domain diagrams and 2D/3D images can be generated through probing the wave speed and energy distribution[73]. Figure 7 presents the representative 1D and 2D UT results of a TC18 alloy sample[117]. Employment of the phased array ultrasonic instead of conventional ultrasonic has significantly improved the signal-to-noise ratio. The ultrasonic method is an emerging NDE approach for detecting the defects inside LPBF printed metals, particularly for the examination of large and complex components due to its excellent portability and high penetration depth. On the other hand, although UT can provide precise location information of pores, it is currently limited by its inadequate quantitative ability[73,117]. Post-processing of data and other evaluation methods should be implemented as complements to improve the detectivity of UT.

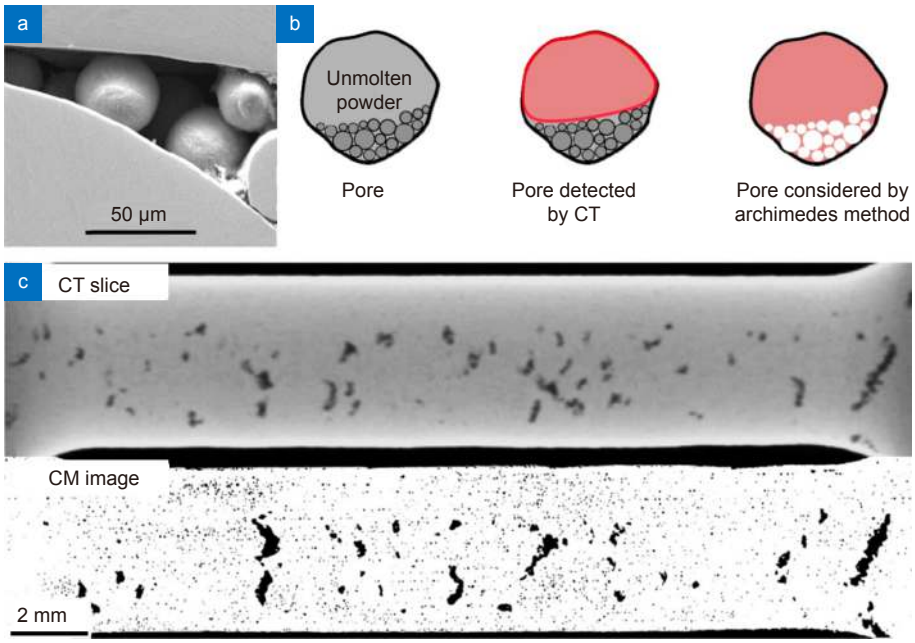

Fig. 6 | Comparative illustration of the limitations of X-ray CT. (**a**) Microscopic image of a LOF pore; (**b**) comparison of pores detected using X-ray CT and the Archimedes method; and (**c**) comparison of the same cross-section in a 316L sample detected by CT and by confocal microscopy (CM). Figure reproduced with permission from: (a, b) ref.[76], Elsevier; (c) ref.[104], under a Creative Commons Attribution-NonCommercial-NoDerivatives 4.0 International License.

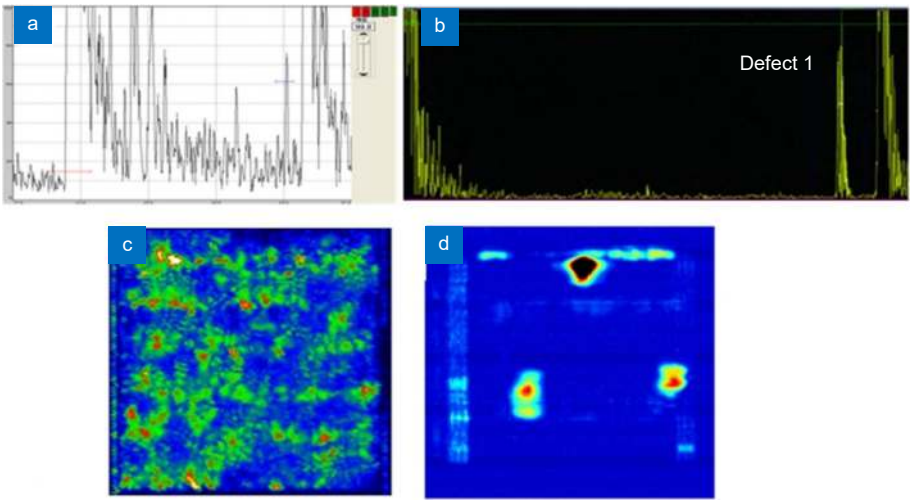

Fig. 7 | 1D ultrasonic A-scan diagrams of (**a**) conventional UT and (**b**) phased array UT; and 2D ultrasonic C-scan images of (**c**) conventional UT and (**d**) phased array UT. Figure reproduced from ref.[117], under a Creative Commons Attribution 4.0 International License.

General effects of porosity on the mechanical performance of LPBF printed metals

The existence of porosity can exert substantial influences on the mechanical performance of metal products[89]. Numerous studies have reported the degradation of mechanical performance that attributed to porosity[18,30,83,118–120]. Whereas, porosity can also be intentionally induced to realize specific functions. For instance, the porous biomedical implants with extra-low elastic modulus[121,122]. Porosity in metals can induce the nucleation of cracks due to the stress concentration under mechanical loads[41,87]. Therefore, the deterioration of ductility and dynamic mechanical performance of LPBF printed metals is often ascribed to the presence of porosity[38,71,123,124]. Meanwhile, the influence and acceptance level of porosity vary from different types of mechanical loads[41,87]. The effects and critical indicators of porosity in different loading situations will be discussed individually in the following subsections.

Tensile properties

Porosity causes reductions in tensile strength and ductility is a general consensus in the studies of cast metals[125,126]. Although LPBF prints products through a way differentiated from the traditional casting, the mechanical effects of porosity do share many similarities among LPBF printed and cast metals[40,126]. As illustrated in Fig. 8(a), the uniform stress field is altered in the adjacent region of an ellipsoidal pore and stress level is elevated near the tip. For an ideal ellipsoidal pore in an isotropic material, the maximum stress, $\sigma_{\max}$, is determined by the tip radius, ρ, and the length of semi-major axis, b, as[127]:

$$\sigma_{\max} = S\left(1+2\sqrt{\frac{b}{\rho}}\right), \tag{4}$$

where S is the remote stress. Stress concentration caused by porosity can deteriorate the mechanical performance of as-printed metals. A representative fractographic image in Fig. 8(b) demonstrates the presence of LOF pores in a LPBF printed Ti–6Al–4V sample with poor strength and ductility.

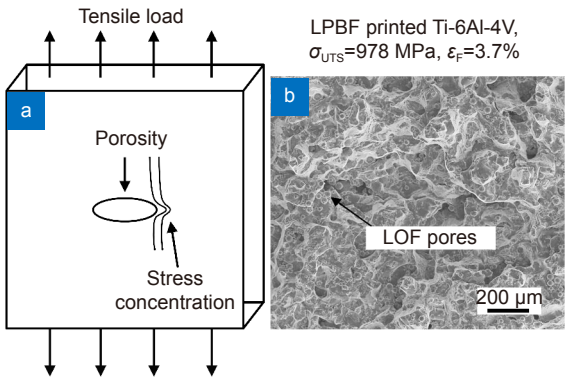

Fig. 8 | Detriments of porosity to the mechanical performance. (**a**) Schematic illustration of uniaxial tensile load applied to a sample with inner porosity; (**b**) fractographic image of a LPBF printed Ti−6Al−4V tensile sample. Figure reproduced with permission from (b) ref.[123], Elsevier.

Uniaxial tensile test is one of the most basic and universal mechanical tests for engineering materials[8,89]. Important mechanical properties, such as yield strength (YS, σ_Y), ultimate tensile strength (UTS, σ_{UTS}), strain at fracture (ε_F), reduction of area (RA), and elastic

modulus (E), can be determined through applying a simple uniaxial tensile force to the sample until it breaks.

Porosity reduces the volume of material that can interact with the applied force. The elastic moduli of porosity-containing materials can be estimated by several empirical models. Bert[128] suggested a model with morphological considerations of porosity based on Rossi's[129] study as:

$$\frac{E}{E_0} = \left[1 - \left(\frac{V_\mathrm{p}}{V_\mathrm{p,max}}\right)\right]^{K_0 V_\mathrm{p,max}}, \tag{5}$$

where E_0 is elastic modulus of fully-dense material, V_p is volume fraction of porosity, $V_\mathrm{p,\,max}$ is geometrically-possible maximum fraction of porosity, and K_0 is stress concentration factor dependent on the morphology of porosity. Previous studies[126,128,130] have validated the feasibility of Eq. 5 to predict the effect of porosity on elastic modulus using both finite element method (FEM) and experiments. The influence of porosity on YS is similar to that on elastic modulus due to similar theoretical analyses at the elastic deformation stage[131,132]. YS decreases with rising porosity fraction owing to the reduction of material as well as the crack initiation at pores. Empirical studies[131,133,134] have also established relationships between porosity fraction and YS of LPBF printed metals that similar to Eq. 5.

Porosity's influence at the plastic deformation stage is much more complicated compared to that at the elastic stage because ductile fracture is inherently anisotropic[41]. Eq. 4 suggests a smaller tip radius causes a higher stress concentration, indicating that the sharpness, or curvature of the tip, plays a dominant role in determining the local stress. Kabir and Richter[90] studied the stress distribution of an LPBF printed Ti–6Al–4V sample with pores in it. Figure 9 presents the FEM simulated stress profile that clearly illustrates the intensified stress nearby pores' sharp tips. During tensile loading, a plastic zone will be generated surrounding a pore's tip before the nominal stress reaches the yield point. The tips of pores can expand and propagate in the corresponding plastic zones, resulting in local plastic deformation and may initiate cracks[41,127].

The ductile fracture behavior of polycrystalline metals is presently explained by the void nucleation, growth, and coalescence mechanism[94,135,136]. A set of microscopic images of void growth–coalescence under uniaxial tensile stress in an Al–Cu–Mg alloy are presented in Fig. 10. The porosity in LPBF printed metals are natural void sites as discussed above. Those pores grow and facilitate

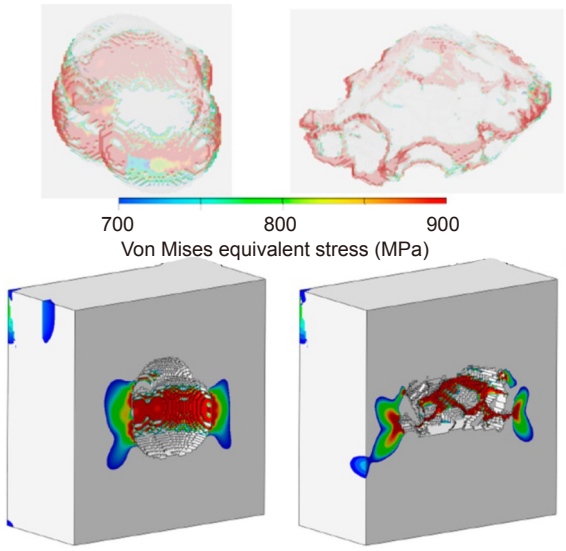

Fig. 9 | Simulated stress distribution profile of two pores in a LPBF printed Ti–6Al–4V sample under identical uniaxial tensile load. Figure reproduced from ref.[90], under a Creative Commons Attribution 4.0 International License.

the void nucleation in their neighborhood during plastic deformation. When two voids become close enough, an internal necking happens at the inter-void ligament and leads to the coalescence of voids[94,137]. Other coalescence mechanisms, such as internal shearing of inter-void ligament and "necklace" coalescence, can also contribute to the void coalescence depending on the strain and distribution of porosity[41,135]. In addition, clustered and periodically-arranged porosity are prone to coalescence owing to the smaller distances between pores and stronger stress triaxiality[41]. Thus, the spatial distribution of porosity can as well influence the mechanical performance significantly. For instance, Yadroitsev et al.[138] reported an apparent correlation between tensile necking and clustered inner pores in an LPBF printed Ti–6Al–4V.

It has been well established that the strain hardening phenomenon dictates the UTS of metals[41,89,139]. Therefore, the elongation at the onset of necking (macroscopic localized strain), a property that closely connected to the porosity[80,94,135], is crucial in determining the engineering UTS of LPBF printed metals. Susmel et al.[140] reported the theory of critical distances (TCD) held a good accuracy in predicting the strength of notched tensile samples, which indicates the detriment increases exponentially against the rising length of pores. Voisin et al.[141] further noted that an LPBF printed Ti–6Al–4V sample with large, clustered subsurface porosity exhibited approximately the same UTS and ductility compared to a sample with porosity fraction two times higher than it.

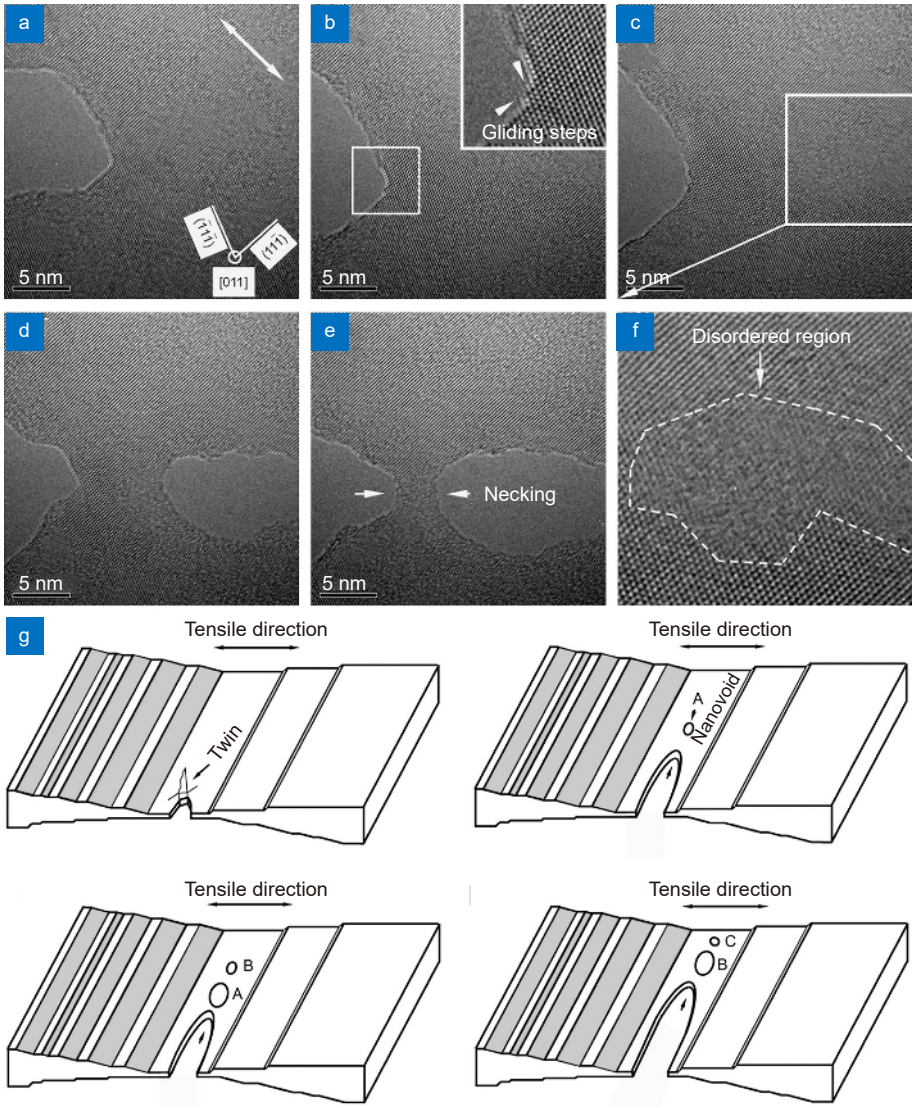

Fig. 10 | Void growth and coalescence under tensile load. (**a**–**f**) High-resolution transmission electron microscopic images presenting the void growth and coalescence during in-situ tensile loading of an Al–Cu–Mg sample, with (**g**) corresponding schematic illustration. Figure reproduced with permission from ref.[136], Elsevier.

Those findings suggest that the periodically-arranged artificial porosity used in functional porous products may cause more harm to the tensile properties than the randomly-arranged porosity. In conclusion, large, sharp, and clustered pores are the most influential types of porosity at the plastic deformation stage.

Along with the increasing strain, the damage accumulates through the interactions of voids till a crack initiates/propagates, or the plastic instability begins[142]. This leads to the localization of strain ("necking") and the decrease of engineering strength[89]. Constitutive yield functions have been proposed by Gurson[143], Tvergaard[144], and Needleman[145], the porosity-related Gurson-Tvergaard-Needleman (GTN) yield function Φ is expressed as[146]:

$$\Phi = \left(\frac{\Sigma}{\sigma_{\rm Y}}\right) + 2q_1 V_{\rm p}^{*} \cdot \cosh\left(\frac{3q_2\Sigma_{\rm m}}{2\sigma_{\rm Y}}\right) - 1 - q_3 V_{\rm p}^{*2}\ , \quad (6)$$

where Σ is the von Mise stress, $\Sigma_{\rm m}$ is hydrostatic stress, q_1, q_2, and q_3 are material constants, and $V_{\rm p}^{*}$ is a function of $V_{\rm p}$. On the basis of yield functions and experimental data, several numerical models have been proposed to predict the correlation between porosity fraction and deformation behaviors[94,135,137,146]. Hao and Brocks[146] incorporated the effects of strain rate and temperature into the GTN model and successfully verified their model using FEM and a 22NiMoCr37 steel sample as presented in Fig. 11.

Haynes[147] developed an simplified empirical model that illustrates the reduction in ductility caused by porosity in sintered metals as:

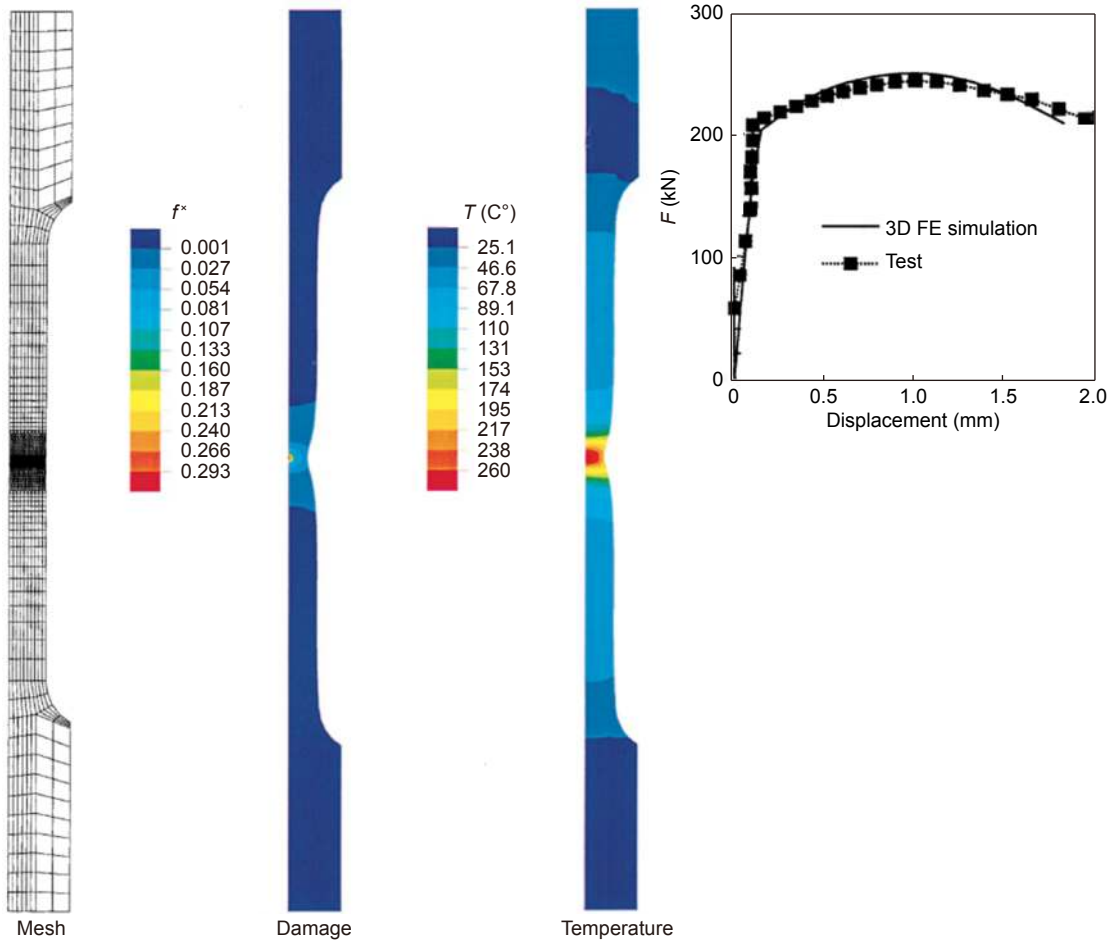

Fig. 11 | FEM simulation of uniaxial tensile tests and corresponding comparison between experimental and predicted data of a 22NiMo-Cr37 steel sample; the mesh is installed with cylindrical voids. Figure reproduced with permission from ref.[146], Springer Nature.

$$\varepsilon_{\mathrm{F}}=\frac{(1-V_{\mathrm{p}})^{\frac{3}{2}}}{(1+CV_{\mathrm{p}}{}^{2})^{\frac{1}{2}}}\varepsilon_{\mathrm{F0}}\ , \tag{7}$$

where C is a material constant, and $\varepsilon_{\mathrm{F0}}$ is strain at fracture of fully-dense material. This model is applicable for preliminary fast estimations.

Fatigue performance

Fatigue failure of metals is caused by the initiation and propagation of fatigue cracks that similar to the last stage of tensile failure after plastic instability occurs[87,148]. Meanwhile, the fatigue cracks are induced by cyclic loadings instead of a simple tension. Two systematic reviews[38,148] have been published recently, focusing on the effects of defects on the fatigue performance of additively manufactured metals. Porosity is one of the most critical roles in determining the fatigue performance of LPBF printed metals because it can serve as fatigue crack initiation sites[148,149]. As depicted in Fig.12, Tammas-Williams et al.[150] illustrated the propagation of porosity-induced fatigue cracks in as-printed Ti–6Al–4V samples.

The size, morphology, and spatial distribution of porosity have received the most research interest since the status of stress concentration generally dominants the fatigue performance of metals[75,87,150–153]. Considering the fact that morphological descriptors of all the pores in a sample are difficult to measure, studies on the effects of porosity on fatigue performance are mainly focused on the size of pores[75,85,86,150,151,154,155]. The maximum pore size has been broadly suggested as the most critical indicator. Statistical tools have been extensively used to estimate the size distribution of porosity[75,85,156–158]. Murakami[159] proposed an empirical model to describe the relationship between stress intensity factor, ΔK_{I}, and the size of spherical pores as:

$$\Delta K_{\mathrm{I}}=0.5\Delta\sigma\sqrt{\pi\sqrt{area}}\ , \tag{8}$$

$$\Delta K_{\mathrm{I}}=0.65\Delta\sigma\sqrt{\pi\sqrt{area}}\ , \tag{9}$$

where $\Delta\sigma$ is stress amplitude. Eq. 8 is for internal pores and Eq. 9 is for surface pores. The stress concentration

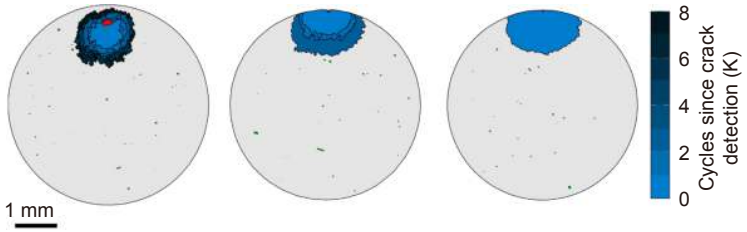

Fig. 12 | Fatigue crack propagation detected by CT in three LPBF printed Ti−6Al−4V samples. The red regions indicate the pores as the initiation sites of fatigue cracks. Figure reproduced with permission from ref.[150], under a Creative Commons Attribution 4.0 International License.

elevates with increasing projected area of pores, indicating a positive scale effect.

The TCD concept has been suggested by Taylor[154] as an effective tool to establish the linkage between porosity and fatigue performance. The material characteristic length, L, is used in TCD models to evaluate the risk of drastic reduction in fatigue limit as:

$$L = \frac{1}{\pi}\left(\frac{K_c}{\sigma_0}\right)^2, \tag{10}$$

where K_c is fracture toughness of material, and σ_0 is characteristic strength of material, which is closely-related to σ_{UTS} and determined experimentally. Defects with length longer than L can exert significantly higher impacts on the fatigue performance as displayed in Fig. 13[154,160]. Taylor[161] further noted a small sample size can lead to a smaller L, indicating the hazard of porosity may aggravate in LPBF printed metals with complex and small structural features. In addition, Caton et al.[162] developed a phenomenological model to correlate the initial pore size and the fatigue life as:

$$\frac{da}{dN} = C_a\left[\left(\varepsilon_{max}\frac{\sigma_a}{\sigma_Y}\right)^s a\right]^t, \tag{11}$$

where a is crack length with the initial value of corresponding pore size, N is number of loading cycles, C_a, s, and t are material constants, ε_{max} is the maximum strain, and σ_a is alternating stress magnitude. The aforementioned findings suggest a promising methodology for estimating fatigue performance directly from porosity descriptors.

LPBF printed metal products are reported to have significantly lower fatigue performance, particularly the high cycle fatigue strength, compared to their wrought counterparts[38,148]. This difference is currently attributed to the defects, the high residual stress, and the non-equilibrium microstructures[38,75,148,163,164], etc. However, two most vital descriptors, namely the irregularity and the largest size of pores, generally increase with rising porosity fraction based on the experimental results[77,81,82,84,165]. The findings above have revealed a potential that a higher porosity fraction may indicate higher probability of fatigue crack initiation and propagation. Therefore, it is possible to develop a constitutive model that correlates porosity fraction with fatigue limit in the future, which will be of great value for quick engineering estimations.

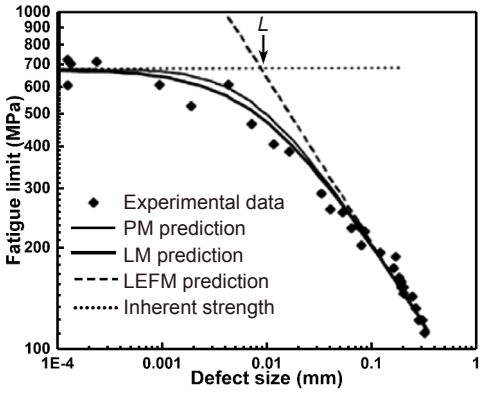

Fig. 13 | Experimental and predicted fatigue limits of silicon carbide samples against defect size. PM, LM, and LEFM are acronyms of point method, line method, and linear elastic fracture mechanics, respectively. Figure reproduced with permission from ref.[154], Elsevier.

Correlation between porosity fraction and tensile properties of representative LPBF printed metals

Mechanical performance is crucial for most engineering metals. Excellent tensile properties are desired in services under heavy/dynamic loads[46,166]. Ti alloys, steels, nickel superalloys, and Al alloys are four major categories of LPBF printed engineering metals at present[8,23,167]. Four most extensively studied materials, namely Ti−6Al−4V, 316L, Inconel 718, and AlSi10Mg, are selected as the representatives of the aforementioned four categories. Their tensile properties at room temperature are discussed along with the influence of porosity. The finish conditions and the methods of density measurement are noted in the tables below to specify the collected data. Cartesian coordinates are employed to represent the

orientations of mechanical tests as shown in Fig. 14. *Z* designates the deposition (building) direction, *X* designates the longitudinal direction perpendicular to *Z*, and *Y* designates the transverse direction perpendicular to both *X* and *Z*.

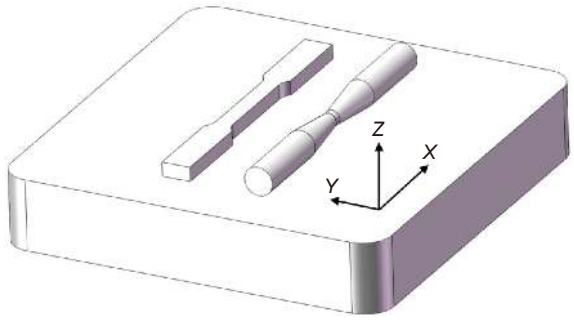

Fig. 14 | Designation of the testing directions.

With the aim of finding general trends and providing a more accessible way to predict the tensile properties, the correlation between tensile properties and porosity volume fraction is fitted using a simple phenomenological model as:

$$y = y_0 \mathrm{e}^{C_\mathrm{P} V_\mathrm{P}} , \tag{12}$$

where y is a specific tensile property (E, σ_Y, σ_UTS, and ε_F), y_0 is fitted y value of fully-dense material, and C_P is a fitted constant that indicates the sensitivity to porosity fraction. The differences in processing parameters, strain rates, and other factors are neglected in this review.

Ti–6Al–4V alloy

Ti–6Al–4V alloy is the most popular Ti alloy (accounts for more than 50% of total Ti usage) that has been vastly used in aerospace, marine, and biomedical industries since the 1950s[168,169]. It is an $\alpha + \beta$ dual-phase alloy with excellent specific strength, good corrosion resistance, and biocompatibility[170]. The LPBF of Ti–6Al–4V alloy has attracted extensive interest due to the challenges in its subtractive machining[170–172]. With the advances in processing optimization, as-printed Ti–6Al–4V components are capable of achieving an excellent combination of strength and ductility without any post treatments[97,123,173].

Tensile properties of the Ti–6Al–4V alloy printed via LPBF are summarized in Table 1. The as-printed Ti–6Al–4V normally contains a high fraction of fine martensitic grains (α′-Ti) that grants high strength to the material[174]. Conventional HTs for LPBF printed Ti–6Al–4V are stress-relief annealing and solution-treated and aging (STA)[97,175]. HTs above the effective martensite decomposition temperature (~780 °C) can transform martensitic phase into more stable $\alpha + \beta$ phases, enhancing the ductility simultaneously[169]. However, the HT-induced decomposition of fine martensites usually decreases the strength of Ti–6Al–4V as presented in Table 1. HIP treatments are capable of eliminating porosity to near-zero, whereas, the simultaneous reduction in strength is ascribed to the high temperature heating (> 1000 °C) during HIP processing[45,97]. Meanwhile, several studies[176,177] reported moderate orientation effects on the tensile properties. The variation of tensile properties for samples built along different directions have been attributed to the inhomogeneity of defects and microstructures. Figure 15 displays the tensile properties against porosity fraction of as-printed Ti–6Al–4V. Phenomenological models are developed as:

$$E = 112.72\mathrm{e}^{-4.63V_\mathrm{P}} , \tag{13}$$

$$\sigma_\mathrm{Y} = 1090.68\mathrm{e}^{-4.08V_\mathrm{P}} , \tag{14}$$

$$\sigma_\mathrm{UTS} = 1208.53\mathrm{e}^{-2.84V_\mathrm{P}} , \tag{15}$$

$$\varepsilon_\mathrm{F} = 8.75\mathrm{e}^{-10.71V_\mathrm{P}} . \tag{16}$$

The mean squared errors (E^2) of fittings are presented in Fig. 15 along with the fitted curves. The tensile properties maintain good when the porosity fraction is suppressed to below 1%. However, ductility of as-printed Ti–6Al–4V appears to be sensitive to both interstitial solutes and porosity fraction. Suppressing the porosity fraction to below 0.5% is necessary for achieving ductile and reliable Ti–6Al–4V products. The YS, UTS, and ductility data spreads significantly, which is probably caused by the variations in interstitial solutes (O, N, C, etc.). Addition of interstitial solutes brings a remarkable hardening effect to Ti–6Al–4V, whereas, the ductility drops significantly once the content of interstitial solutes exceeds a certain critical limit[178,179].

316L stainless steel

316L SS is the second-most used austenitic SS after 304 SS[184]. The primary alloying elements of 316L SS are Cr (16–18 wt.%), Ni (10–12 wt.%), and Mo (2–3 wt.%). 316L exhibits excellent ductility and weldability under multiple finish conditions[184–186]. It has been extensively used in chemical, food processing, marine, and biomedical industries due to its reasonable cost, fine formability, and good resistance to corrosion/oxidation[185–187]. A major drawback of conventionally-formed 316L is the low

Table 1 | Summarized tensile properties of LPBF printed Ti−6Al−4V samples. Data not available is marked as NA.

Condition	Sample orientation	Method	Porosity fraction (vol.%)	*E* (GPa)	YS (MPa)	UTS (MPa)	ε_F (%)	Ref.
As-printed	*Z*	Archimedes	0	109 ± 2.1	1098 ± 15	1237 ± 13	8.8 ± 0.6	ref.[123]
			1	111 ± 1.4	1150 ± 91	1257 ± 74	8.0 ± 2.0	
			5	95 ± 3.0	932 ± 16	1112 ± 13	6.6 ± 1.4	
			1	109 ± 3.7	1066 ± 91	1148 ± 80	5.4 ± 3.8	
			5	84 ± 3.0	813 ± 23	978 ± 32	3.7 ± 0.6	
As-printed	NA	Archimedes	0.3 ± 0.1	110 ± 5	990 ± 5	1095 ± 10	8.1 ± 0.3	ref.[180]
Annealed			0.3 ± 0.1	117 ± 1	870 ± 15	990 ± 15	11.0 ± 0.5	
As-printed	*X*	Archimedes	1	105 ± 5	1137 ± 20	1206 ± 8	7.6 ± 2	ref.[176]
Annealed				101 ± 4	965 ± 16	1046 ± 6	9.5 ± 1	
As-printed	*Y*			102 ± 7	962 ± 47	1166 ± 25	1.7 ± 0.3	
Annealed				110 ± 29	900 ± 101	1000 ± 53	1.9 ± 0.8	
As-printed	*X*	CT	0.1	112 ± 2.1	1098 ± 2	1265 ± 4.8	9.4 ± 0.42	ref.[173]
Annealed				117 ± 2.2	1098 ± 4.8	1170 ± 5.7	10.9 ± 0.75	
Annealed	*Z*	Archimedes	4.4	NA	710	760	NA	ref.[76]
			1.6		868	944		
As-printed	*Z*	2D	0.077	112.4	986	1155	10.9	ref.[97]
Annealed (700 °C)				117.4	1051	1115	11.3	
Annealed (900 °C)				118.8	908	988	9.5	
HIP			0.012	115.4	885	973	19.0	
As-printed	*X*	Archimedes	0.8	NA	1273 ± 23	1421 ± 120	3.2 ± 0.5	ref.[181]
	Z				1150 ± 67	1246 ± 134	1.4 ± 0.5	
HIP	*Z*	CT	0	NA	912	1005	8.3	ref.[45]
As-printed	*X*	2D	0.6 ± 0.2	119 ± 7	967 ± 10	1117 ± 3	8.9 ± 0.4	ref.[182]
Annealed				117 ± 6	937 ± 9	1052 ± 11	9.6 ± 0.4	
As-printed	*Z*	2D	5	NA	1056 ± 29	1351 ± 34	5.5 ± 0.8	ref.[175]
Annealed					1098 ± 41	1181 ± 9	5.0 ± 0.1	
As-printed	*X*	2D	0.45	NA	1050	1230	4.8	ref.[183]
	Z		0.28		1021	1186	7.7	
HIP	*X*		0		994	1083	12.7	
	Z				926	990	15.8	

YS (~250−300 MPa) since it cannot be hardened through quenching[186,188]. However, hierarchical, heterogeneous microstructures have been discovered in the LPBF printed 316L, granting an encouraging high YS to the material[186,187]. The scope of this classical engineering metal is expanding with the assistance of LPBF.

Tensile properties of the 316L SS printed via LPBF are summarized in Table 2. The hierarchical cellular microstructure generated through LPBF printing is critical to realize high strength, thus, the conventional HT is a simple stress-relief/solution annealing to maintain most of the as-printed microstructural features[189]. Similar to the Ti−6Al−4V alloy, 316L SS printed using proper parameters exhibits excellent tensile properties without any post treatments. Mechanical anisotropy has been noted in samples printed along different directions[190−192]. These variations have been ascribed to the anisotropic microstructure, textures, and defects[190,191]. A general trend of strength−ductility trade-off appears in those high-density 316L SS samples. High laser energies as well as high-temperature HTs can improve the ductility, whereas, it may reduce the density of dislocations and thus the YS[187,193]. Therefore, HIP becomes a less-favorable post treatment due to its possible damage to the YS. Figure 16 displays the tensile properties against porosity fraction of as-printed 316L SS. Phenomenological models are developed as:

$$E = 204.48\mathrm{e}^{-3.65V_\mathrm{P}}\ , \tag{17}$$

$$\sigma_\mathrm{Y} = 597.33\mathrm{e}^{-5.21V_\mathrm{P}}\ , \tag{18}$$

$$\sigma_\mathrm{UTS} = 730.72\mathrm{e}^{-5.52V_\mathrm{P}}\ , \tag{19}$$

$$\varepsilon_\mathrm{F} = 51.70\mathrm{e}^{-31.54V_\mathrm{P}}\ . \tag{20}$$

The mean squared errors of fittings are presented in

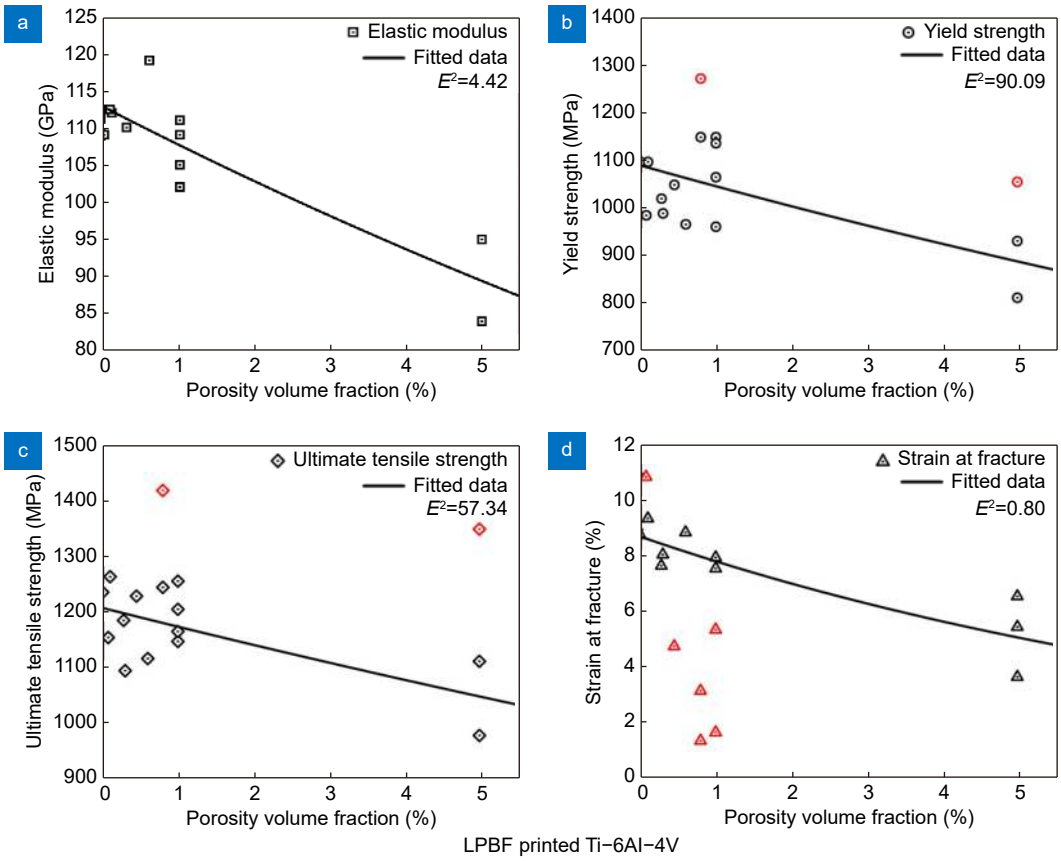

Fig. 15 | Summarized tensile properties of LPBF printed Ti−6Al−4V versus porosity fraction, with corresponding phenomenological models. The red data spots are outliers that excluded from fitting.

Fig. 16 along with the fitted curves. As depicted by Eq. 20, the ductility of as-printed 316L is highly-sensitive to porosity fraction. A nearly 40% reduction in ductility has been observed in the samples with ~1% porosity fraction compared to the fully-dense samples. To achieve excellent ductility and UTS, the porosity fraction should be suppressed to below 1% for as-printed 316L SS. The spreads of data in low-porosity-fraction areas are mainly caused by the microstructural anisotropy[191,194,195]. The columnar grains that grow along the deposition direction may decrease the strength of 316L samples printed along Z direction due to a lower density of grain boundaries.

Inconel 718 superalloy

Inconel 718 superalloy is a Ni–Fe–Cr based superalloy with a nominal chemical composition of Fe–51Ni–19Cr–5Nb–3Mo–1Co–1Ti–xAl (in wt.%)[200,201]. It maintains outstanding strength, fatigue life, and resistance to oxidation/corrosion up to 700 °C, making this material an excellent choice for high-temperature applications[201,202]. Inconel 718 is particularly favored in fabricating gas turbines, combustors, and high pressure vessels[200,202,203]. As reported by Paulonis and Schirra[204], the alloy can make up over half the total weight of a modern aircraft turbofan engine. On the other hand, the high strength at elevated temperatures as well as the low thermal conductivity of Inconel 718 hinders its forging and cold machining[201]. AM technologies including LPBF have been therefore vastly employed in the fabrication of complex Inconel 718 components[202,205–208]. The γ' (Ni_3(Al, Ti)) and γ'' (Ni_3Nb) precipitates are dominating roles in determining the mechanical performance of Inconel 718 products[209]. Proper HTs are essential for LPBF printed Inconel 718 to achieve ideal properties[203,207,209].

Tensile properties of Inconel 718 printed via LPBF are summarized in Table 3. The STA treatment, for instance, that recommended by AMS 5662[210], has long been used as a standard HT for Inconel 718 products[203–205]. This HT also works well with LPBF printed Inconel 718, generating a significant precipitation hardening effect while suppressing the detrimental Laves phase[211]. Anisotropic microstructure and mechanical performance have been observed. Notable fluctuations in elastic modulus and YS

Table 2 | Summarized tensile properties of LPBF printed 316L SS samples. Data not available is marked as NA.

Condition	Sample orientation	Method	Porosity fraction (vol.%)	*E* (GPa)	YS (MPa)	UTS (MPa)	ε_F (%)	Ref.
As-printed	*Z*	Archimedes	0.2	NA	487 ± 3	594 ± 4	49 ± 4	ref.[187]
HIP			0		220	570	54	
As-printed	*X*	Archimedes	0.5	NA	648	744.8	52.5	ref.[196]
As-printed	*X*	NA	0.05	NA	562.5 ± 6.7	616.6 ± 8.1	24.2 ± 3.0	ref.[190]
	Z				572 ± 8.3	635.9 ± 6.2	38.6 ± 2.8	
As-printed	*X*	Archimedes	1	173 ± 8	648 ± 4	772 ± 5	24.8 ± 0.3	ref.[194]
	Z			190 ± 17	588 ± 10	720 ± 12	29.0 ± 2.9	
As-printed	*X*	2D	2.5 ± 1.0	NA	534 ± 5.7	653 ± 3.4	16.2 ± 0.8	ref.[192]
	Y		3.3 ± 1.0		528 ± 3.9	659 ± 3.2	16.6 ± 0.4	
	Z		6.2 ± 2.6		444 ± 26.5	567 ± 18.6	8 ± 2.9	
As-printed	NA	Archimedes	0.3	NA	637.9 ± 11.3	751.6 ± 15.9	41.2 ± 2.7	ref.[193]
Annealed (1050 °C)					423.8 ± 8.4	672.8 ± 13.4	43.9 ± 3.1	
Annealed (1200 °C)					415.7 ± 9.1	683.9 ± 16.4	51.6 ± 2.6	
As-printed	*X*	2D	1.31 ± 0.20	NA	473.1 ± 8.4	610.1 ± 7.7	35.5 ± 3.4	ref.[185]
			0.06 ± 0.02		487.1 ± 7.2	618.6 ± 436	55.7 ± 2.5	
As-printed	*X*	2D	1.54 ± 0.49	167 ± 12	609 ± 43	681 ± 7	28.9 ± 3.9	ref.[195]
	Z		0.85 ± 0.27	152 ± 7	490 ± 2	612 ± 2	21.4 ± 1.6	
As-printed	*X*	2D	2.5 ± 1.0	NA	534 ± 6	653 ± 3	16.2 ± 0.8	ref.[177]
	Y		3.3 ± 1.0		528 ± 4	659 ± 3	16.6 ± 0.4	
	Z		6.2 ± 2.6		444 ± 27	567 ± 19	8 ± 2.9	
As-printed	*Z*	2D	0.41	NA	541.75	653.15	56.45	ref.[197]
			0.08		531.1	632.1	59.2	
			0.07		453.1	556.7	63.6	
As-printed	*X*	2D	4.8	NA	417 ± 19	481 ± 23	18.5 ± 3.2	ref.[198]
	Z				416 ± 18	454 ± 12	9.7 ± 3.8	
As-printed	*Z*	CT	0.2	219 ± 41	517 ± 38	687 ± 40	32 ± 5	ref.[191]
Annealed	*Z*			212 ± 44	463 ± 34	687 ± 37	25 ± 8	
	X			169 ± 22	454 ± 52	750 ± 8	29 ± 2	
	XZ (45°)			190 ± 58	440 ± 52	662 ± 24	28 ± 3	
	XYZ (45°)			186 ± 52	409 ± 64	674 ± 10	26 ± 3	
As-printed	*Z*	Archimedes	1.2	190	422	NA	NA	ref.[199]
			1.3	183	467			
			1.3	184	437			
			5.1	173	345			

have been detected for both as-printed and STA-treated samples[212–215], indicating the elastic modulus of as-printed Inconel 718 is highly-sensitive to processing parameters (sample orientations, laser energy density, etc.). Considering the STA treatment is essential for the hardening of Inconel 718, Fig. 17 displays the tensile properties against porosity fraction of STA-treated Inconel 718 superalloy. Phenomenological models are developed as:

$$\sigma_Y = 1228.74\mathrm{e}^{-5.38V_P}, \quad (21)$$

$$\sigma_{UTS} = 1422.53\mathrm{e}^{-4.45V_P}, \quad (22)$$

$$\varepsilon_F = 15.63\mathrm{e}^{-19.87V_P}. \quad (23)$$

The mean squared errors of fittings are presented in Fig. 17 along with the fitted curves. The number of elastic modulus data spots is not enough for a reasonable fitting, thus the model of *E* is omitted for Inconel 718. A porosity fraction below 0.5% is possibly suitable for LPBF printed Inconel 718 to realize excellent tensile properties. The trend of tensile properties are similar to that of 316L. The YS and UTS drop near-proportionally against elevating porosity fraction. The ductility of STA-treated Inconel 718 is less sensitive to the porosity fraction compared to that of as-printed 316L. In addition, the spreads of elastic modulus and ductility data are high in the low-porosity-fraction areas. Therefore, the

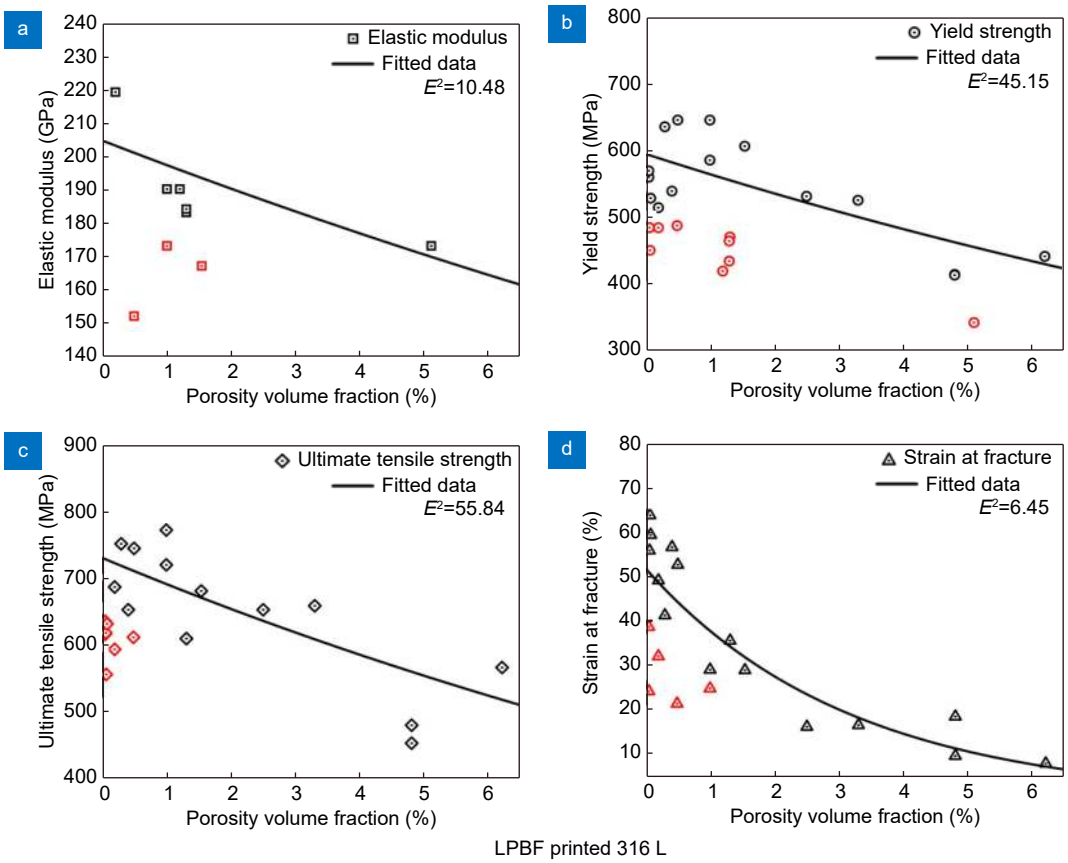

Fig. 16 | Summarized tensile properties of LPBF printed 316L SS versus porosity fraction, with corresponding phenomenological models. The red data spots are outliers that excluded from fitting.

microstructural factors are probably the dominating roles in determining the mechanical performance of Inconel 718 when the porosity fraction is below 1%.

AlSi10Mg alloy

Al alloys are renowned as light-weight engineering metals[221]. AlSi10Mg alloy is traditionally a cast Al alloy that can be hardened through HTs[221–223]. It has been extensively employed to fabricate light-weight components in the automobile and aerospace industries, owing to its good strength, weldability, and limited thermal expansion[48,222–224]. With the development of LPBF technology, crack-free AlSi10Mg products have been successfully printed without adding nucleants, implying a further extension of its application[223–225].

Tensile properties of AlSi10Mg alloy printed via LPBF are summarized in Table 4. Solution + peak aging HT (STA, T6) is commonly applied to cast AlSi10Mg to induce Mg_2Si precipitates[48]. However, this hardening method has not shown significant effect on LPBF printed AlSi10Mg samples[48,222,226]. The strength–ductility trade-off is a common trend in heat-treated AlSi10Mg samples[227]. Chen et al.[228] ascribed the high strength of as-printed AlSi10Mg to the hierarchical microstructure that induced by LPBF processing, which is similar to the LPBF printed 316L SS[186]. Girelli[48] reported a notable increase in the porosity fraction after 510–540 °C HT. The growth of pores is probably caused by the thermal expansion of entrapped gas since the reduction in density elevates with increasing peak temperature and heating time. In addition, several works[57,229–231] suggested that the mechanical anisotropy of as-printed AlSi10Mg can be effectively eliminated by HTs at 300 °C or above. Figure 18 displays the tensile properties against porosity fraction of as-printed AlSi10Mg alloy. Phenomenological models are developed as:

$$E = 73.02\mathrm{e}^{-6.74V_\mathrm{P}}\,, \tag{24}$$

$$\sigma_\mathrm{Y} = 256.66\mathrm{e}^{-11.14V_\mathrm{P}}\,, \tag{25}$$

$$\sigma_\mathrm{UTS} = 395.37\mathrm{e}^{-10.30V_\mathrm{P}}\,, \tag{26}$$

$$\varepsilon_\mathrm{F} = 6.26\mathrm{e}^{-62.79V_\mathrm{P}}\,. \tag{27}$$

The mean squared errors of fittings are presented in Fig. 18 along with the fitted curves. As depicted by Eq. 27, AlSi10Mg is a relatively-brittle material in comparison to Ti–6Al–4V, 316L, and Inconel 718. The ductility of

Table 3 | Summarized tensile properties of LPBF printed Inconel 718 samples. Data not available is marked as NA.

Condition	Sample orientation	Method	Porosity fraction (vol.%)	*E* (GPa)	YS (MPa)	UTS (MPa)	ε_F (%)	Ref.
As-printed	*Z*	2D	0.1	NA	580	845	19	ref.[205]
ST					535	870	34	
STA					1240	1400	9.6	
HIP					430	875	38	
HIP+A					1100	1315	15	
As-printed	*Z*	NA	0.48	NA	711 ± 14	1110 ± 11	24.5 ± 1.1	ref.[216]
	X				858 ± 12	1167 ± 10	21.5 ± 1.3	
STA	*X*	NA	0.3	NA	1295	1484	NA	ref.[207]
	XZ (45°)				1368	1521		
	Z				1240	1398		
STA	*X*	2D	5.43	192.3 ± 32.0	916 ± 14	1112 ± 15	3.24 ± 0.13	ref.[217]
As-printed	*X*	2D	0.11	173 ± 13	668 ± 16	1011 ± 27	22 ± 2	ref.[213]
			0.27	113 ± 3	531 ± 9	866 ± 33	21 ± 7	
STA	*X*	CT	0.03	195	1290	NA	11	ref.[214]
	XZ (45°)		0.11	215	1305		9.5	
	Z		0.15	165	1215		9	
HIP	NA		0	200	1125		18.6	
As-printed	*X*	Archimedes	0	204	898	1143	22.6	ref.[218]
STA				201	1132	1319	16	
STA	*X*	Archimedes	0.14 ± 0.06	NA	1213	1427	9.3	ref.[210]
			0.15 ± 0.16		1234	1455	19.2	
			0.16 ± 0.18		1213	1434	10.2	
			0.16 ± 0.18		1213	1420	6.9	
			0.18 ± 0.07		1213	1420	6.9	
			0.29 ± 0.18		1179	1475	13.9	
			0.30 ± 0.22		1213	1455	10.8	
			0.43 ± 0.49		1207	1448	12.2	
			0.92 ± 1.36		1207	1372	3.6	
			1.03 ± 1.59		1207	1455	14.5	
			2.84 ± 5.77		1220	1406	5.7	
			8.47 ± 4.98		1179	1358	4.4	
STA	*Z*	2D	0.48	NA	1100	1360	17.5	ref.[219]
			1.35		1120	1340	19.8	
As-printed	NA	Archimedes	0.9	NA	770.5 ± 2.1	1064.5 ± 3.5	22.35 ± 0.21	ref.[220]
			0.9		772.5 ± 2.2	1065.0 ± 1.4	25.25 ± 0.35	
			1.33		804.0 ± 49.5	1076.5 ± 28.9	16.85 ± 0.07	
			1.14		800.5 ± 7.1	1075.0 ± 8.5	21.05 ± 0.21	
As-printed	*Z*	NA	0.2	162 ± 18	572 ± 44	904 ± 22	19 ± 4	ref.[215]
	X			193 ± 24	643 ± 63	991 ± 62	13 ± 6	
	XZ (45°)			200 ± 23	590 ± 15	954 ± 10	20 ± 1	
	XYZ (45°)			208 ± 48	723 ± 55	1117 ± 45	16 ± 3	
STA	*Z*			163 ± 30	1074 ± 42	1320 ± 6	19 ± 2	
	X			199 ± 15	1159 ± 32	1377 ± 66	8 ± 6	
	XZ (45°)			188 ± 19	1152 ± 24	1371 ± 5	15 ± 5	
	XYZ (45°)			209 ± 44	1241 ± 68	1457 ± 55	14 ± 5	
As-printed	*X*	2D	0.16	216.5 ± 3.7	754.3 ± 4.4	1070.5 ± 11.6	20.5 ± 0.8	ref.[212]
	Z			211.5 ± 4.7	659.4 ± 19.2	1018.9 ± 0.8	23.9 ± 0.5	
	XZ (45°)			213.4 ± 2.7	704.2 ± 5.1	1045 ±.8 5	20.2 ± 0.2	

Table 3 (Continued)

Condition	Sample orientation	Method	Porosity fraction (vol.%)	*E* (GPa)	YS (MPa)	UTS (MPa)	ε_F (%)	Ref.
As-printed	*Z*	2D	0.23	NA	698.2 ± 15.2	995.2 ± 12.8	33.21 ± 1.1	ref.[211]
STA			0.25		1237.8 ± 13.4	1379.3 ± 10.4	19.49 ± 0.54	
STA			0.23		1203.3 ± 5.5	1390.2 ± 8.1	21.96 ± 0.37	
HIP + STA			0.1		1087.2 ± 7.5	1384.7 ± 6.2	23.36 ± 0.62	
HIP + STA			0.11		1110.9 ± 7.4	1395.7 ± 4.2	23.61 ± 0.36	

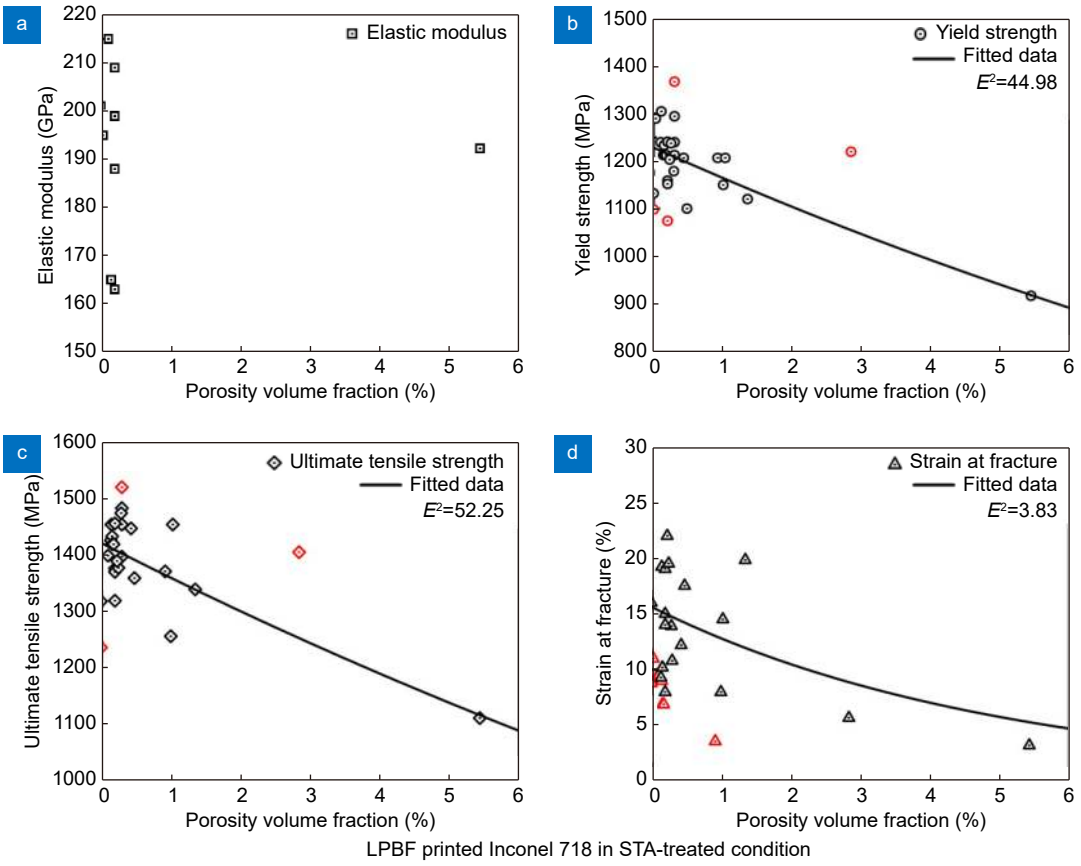

Fig. 17 | Summarized tensile properties of LPBF printed Inconel 718 versus porosity fraction, with corresponding phenomenological models. The red data spots are outliers that excluded from fitting.

as-printed AlSi10Mg is extremely sensitive to the porosity fraction. Fatal cracks may initiate from the pores at an early stage of tensile deformation, resulting in high spreads of ductility and UTS data. To conclude, the elimination of porosity is vital for less-ductile metals such as LPBF printed AlSi10Mg[41,229,232]. The porosity fraction of as-printed AlSi10Mg should be as low as possible (< 0.1%) to reduce the risk of crack initiation.

Comparison of tensile properties between LPBF printed metals and their traditionally-fabricated, porosity-free counterparts

The optimal tensile properties of the four aforementioned LPBF printed metals are summarized in Table 5, along with those of their porosity-free wrought/cast counterparts. Ti–6Al–4V, 316L, and Inconel 718 printed under optimized processes exhibit apparently superior YS and UTS than their wrought counterparts. The as-printed AlSi10Mg lacks Mg_2Si precipitates, leading to a slightly lower YS compared to that of STA-T6-treated cast AlSi10Mg. The ductility of as-printed Ti–6Al–4V and Inconel 718 has reduced simultaneously as expenses for hardening. Nevertheless, the ductility of as-printed 316L and AlSi10Mg has been enhanced owing to the unique hierarchical microstructures generated by LPBF processing. All four LPBF printed metals hold elastic moduli that comparable to their wrought/cast counterparts when the porosity fraction has been suppressed to near-zero. However, the anisotropic elastic moduli

Table 4 | Summarized tensile properties of LPBF printed AlSi10Mg samples. Data not available is marked as NA.

Condition	Sample orientation	Method	Porosity fraction (vol.%)	*E* (GPa)	YS (MPa)	UTS (MPa)	ε_F (%)	Ref.
As-printed	*X*	Archimedes	0	NA	264 ± 4	452 ± 1	8.6 ± 1	ref.[48]
	Z				247 ± 1	482 ± 1	6.5 ± 0.3	
STA (T6)	*X*		2.31		277 ± 1	332 ± 1	5.8 ± 0.2	
	Z				248 ± 14	299 ± 24	5.1 ± 1.1	
As-printed	*X*	Archimedes	5.67	NA	NA	248	NA	ref.[233]
			0.71			330		
As-printed	*X*	2D	0	NA	327	470	8	ref.[234]
As-printed	*X*	CT	0.01	NA	241.2 ± 1.0	379.6 ± 4.5	8.1 ± 0.4	ref.[229]
	XZ (45°)		0.06		239.1 ± 6.2	367.8 ± 4.4	5.7 ± 0.8	
	Z		0.08		236.8 ± 6.2	351.8 ± 6.5	8.3 ± 0.3	
As-printed	*X*	2D	1	NA	NA	282.2	NA	ref.[226]
						353.3		
STA (T6)	*Z*					343.1		
						330		
As-printed 300 °C pre-heated	*X*					248.9		
						270		
STA (T6) 300 °C pre-heated	*Z*					353.1		
						341.1		
Annealed (300 °C)	*X*	Archimedes	1.87	71.3	168	267	8.6	ref.[231]
				69.0	170	267	9.5	
	Z			70.3	170	272	7.8	
				70.1	170	277	8.7	
				69.5	168	273	8.2	
				73.0	167	269	8.0	
Annealed (300 °C)	*ZX*	Archimedes	0.02	NA	180	287	14.3	ref.[57]
					182	285	17.9	
Annealed (300 °C) + shot peened	*X*	Archimedes	0.08	73	243 ± 7	330 ± 3	6.2 ± 0.3	ref.[230]
	Z		0.07	72	231 ± 3	329 ± 2	4.1 ± 0.2	
As-printed	*X*	Archimedes	0.6	68 ± 3	NA	396 ± 8	3.5 ± 0.6	ref.[232]
Aged (175 °C)				66 ± 5		399 ± 7	3.3 ± 0.4	
As-printed	*Z*	2D/CT	1.73	NA	215	275	1.3	ref.[222]
			0.25		225	297	1.65	
			2		206	280	1.48	
STA (T6)			1.1		213	225	1.1	
As-printed	*X*	NA	0.06	77 ± 5	268 ± 2	292 ± 4	1.4 ± 0.3	ref.[230]
STA (T6)				73 ± 4	239 ± 2	333 ± 15	3.9 ± 0.5	
As-printed	*X*	Archimedes	1.5	68 ± 3	NA	391 ± 6	5.55 ± 0.4	ref.[235]
	Z			NA		396 ± 8	3.47 ± 06	

discovered in as-printed 316L and Inconel 718 demand extra attention in applications[191,194,195,212–215]. In summary, the tensile properties of LPBF printed metals can be comparable to, even superior to those of the traditionally-fabricated, porosity-free counterparts. Suppressing the porosity fraction to certain acceptance levels is essential for achieving excellent mechanical performance. On the other hand, metals with high porosity fractions may be intentionally printed to pursue lower moduli.

Controlling the porosity in LPBF printed metals

The relative density of LPBF printed metal products has always been a primary metric to evaluate their usability. As displayed in the sections above, the presence of high porosity fraction or large-scale porosity exhibits substantial detriment to the mechanical performance. Products with minimum fraction of porosity are generally preferred for their better performance and reliability.

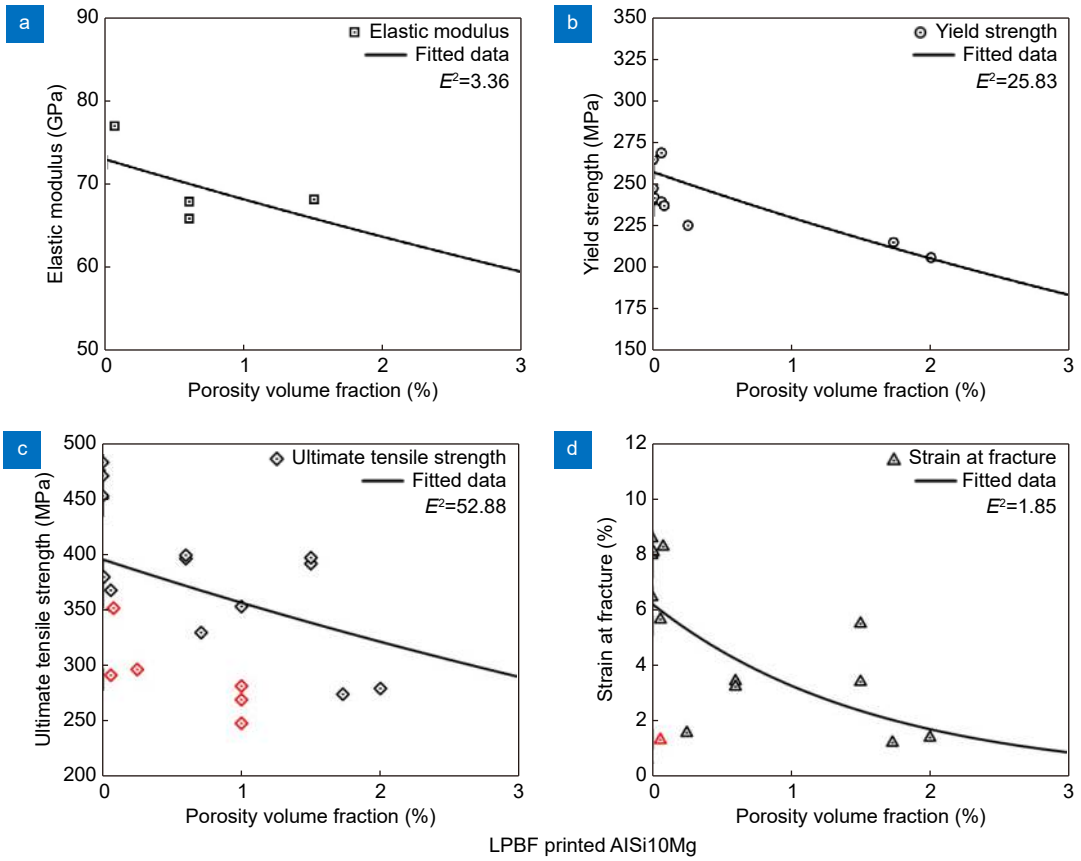

Fig. 18 | Summarized tensile properties of LPBF printed AlSi10Mg versus porosity fraction, with corresponding phenomenological models. The red data spots are outliers that excluded from fitting.

Table 5 | Summarized optimal tensile properties of LPBF printed Ti−6Al−4V, 316L, Inconel 718, and AlSi10Mg samples, as well as their porosity-free counterparts. Data not available is marked as NA.

Material	Condition	Porosity fraction (vol.%)	*E* (GPa)	YS (MPa)	UTS (MPa)	ε_F (%)	Ref.
Ti−6Al−4V	Wrought	0	108.2	944	1045	24.7	ref.[236]
	As-printed (optimal)	0.1	112 ± 2.1	1098 ± 2	1265 ± 4.8	9.4 ± 0.42	ref.[173]
	Predicted (optimal)	0	112.72	1090.68	1208.53	8.75	This work
316L	Wrought	0	200	255−310	535−623	30−40	ref.[237]
	As-printed (optimal)	0.2	NA	637.9 ± 11.3	751.6 ± 15.9	41.2 ± 2.7	ref.[193]
	Predicted (optimal)	0	204.48	597.33	730.72	51.70	This work
Inconel 718	Wrought + STA	0	200−211	1048−1138	1317−1348	19−21	ref.[215]
	As-printed + STA (optimal)	0.2	209 ± 44	1241 ± 68	1457 ± 55	14 ± 5	ref.[215]
	Predicted (optimal)	0	NA	1228.74	1422.53	15.63	This work
AlSi10Mg	High-pressure die cast + STA (T6)	0	71	285−330	330−365	3−5	ref.[238]
	As-printed (optimal)	0.08	NA	264 ± 4	452 ± 1	8.6 ± 1	ref.[48]
	Predicted (optimal)	0	73.02	256.66	395.37	6.26	This work

Samples printed using matured materials, such as Ti−6Al−4V and AlSi10Mg, are capable of achieving near-full density and excellent performance. Whereas, challenges still exist in the LPBF processing of refractory, brittle metals, and metal matrix composites[67,239]. To suppress the porosity in as-printed metals is crucial yet beneficial for the repeatable fabrication of high-quality products. The porosity controlling methods can be divided into three primary categories at present: the processing optimization, the post treatments, and the online monitoring.

Processing optimization

Processing optimization is the most accessible approach

to suppress porosity formation[166,240]. This optimization is frequently performed as an initial step of studies on LPBF.

Yadroitsev et al.[240] suggested three major categories of processing variables: the feedstock powder, the laser parameters, and the strategy of manufacturing. The granulometry and morphology of feedstock powder are predominant roles in determining the properties of as-paved powder bed[241,242]. Using feedstock powder with good flowability and proper size distribution can pave a denser and more homogeneous powder bed, resulting in less porosity after printing[31].

Most commercially-available LPBF machines allow certain customization/adjustments to the processing parameters. Laser power, scanning velocity, hatch spacing, and layer thickness are parameters that have been mostly adjusted[224,232,243]. Figure 19 illustrates the significant variation in molten pools that generated through adjusting the aforementioned parameters. The optimization of laser parameters can contribute considerably to the stabilization of molten pool[19,29]. Hence, ideal melting tracks combined with proper overlap rates are essential for eliminating the processing-induced porosity[244]. Numerical methods, particularly the FEM simulations, have shown great potential in guiding the processing optimization[28,245,246]. Khairallah et al.[28] performed multiphysics, high-fidelity LPBF simulations on Ti–6Al–V and 316L, using an advanced full-laser-ray-tracing heat source. An optimized laser power map to reduce spatter and porosity has been proposed based on their simulations. However, such high-fidelity simulations demand enormous computing power and extremely-complicated modeling. Current high-fidelity simulations are mostly limited to a single track or a single layer[247]. Substantial improvements in processing parameters demand for practical multi-track and multi-layer simulations, which are presently at an initial yet promising stage[248,249].

Other parameters of manufacturing, such as the preheating temperatures, the scanning patterns, the orientations to place components, and the speed/blowing direction of shielding gas, can be further utilized to suppress the porosity. Adjusting these minor parameters lead to varied thermal behaviors, which may influence the melting[177,233,250,251]. Anwar and Pham[233] reported notable

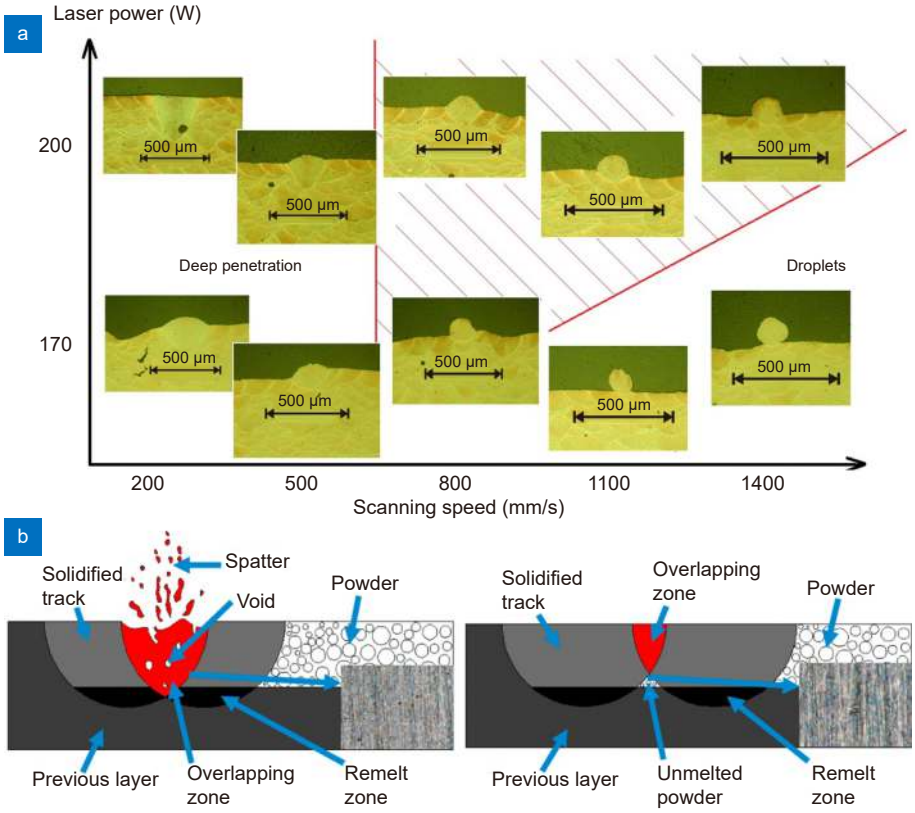

Fig. 19 | The influence of LPBF processing parameters. (**a**) Cross-sections of single scan tracks of LPBF printed AlSi10Mg; (**b**) schematic illustration of the porosity formation due to inappropriate overlap rates. Figure reproduced with permission from: (a) ref.[232], Taylor & Francis; (b) ref.[244], Elsevier.

differences in the amount of laser spatter for samples printed along different directions. Extra attention should be paid to these minor processing parameters when printing materials that are prone to forming porosity.

Post treatments

HTs and machining after LPBF printing are capable of reducing the porosity fraction. Owing to the entrapped gas in pores, pressure-less HTs are generally not feasible for the elimination of porosity[45–47]. Thermal expansion of entrapped gas may even induce porosity growth in less-stiff materials[47,48]. HIP treatment has been employed in casting and PM for over 60 years to reduce the inner voids[31]. This treatment applies high isostatic pressure to the products via the surrounding medium (usually inert gases) at elevated temperatures[252]. Heating and pressing facilitate the closure of void-type defects thorough lowering the YS while raising the diffusivity[253]. Proper HIP treatments can significantly increase the ductility of LPBF printed metals[183,187,205,254]. The strength, in particular UTS, may also increase after HIP due to the densification and elongated strain-hardening stage[76]. Substantial improvements in fatigue performance have been reported for LPBF printed less-ductile metals after HIP[45,255–257]. However, the benefit on fatigue performance disappears for the dense and ductile LPBF printed 316L SS[256]. This phenomenon is probably caused by the microstructural evolution and corresponding loss in strength after HIP. The heating of HIP can induce grain growth, decomposition of nonequilibrium phases, and reduction in dislocation density[253]. Therefore, the parameters of HIP request elaborate optimization to achieve positive influences.

Surface and near-surface defects can be removed by post subtractive machining. Samples with polished surfaces always exhibit better fatigue performance than those with rough surfaces since the surface defects hold the highest probability of crack initiation[38,75,153]. The hybrid additive manufacturing technology has emerged in recent years as a promising tool for in-situ defect elimination[258,259]. Products can be printed and then precisely machined within a hybrid machine, saving considerable time and labor cost. With the guidance of evaluation tools (e.g. CT), the subtractive methods can be more effective in eliminating porosity and other near-surface defects.

Online monitoring

The online (or in-situ) monitoring of LPBF processing has attracted intense research interest in recent years[29,260–262]. Optical sensors, pyrometers, thermocouples, and other sensors have been implemented for the real-time monitoring of processing[262]. The online monitoring technologies provide more information, particularly on the laser–matter interactions and the melting/solidification behaviors, than the traditional offline measurements[263,264]. The formation, dimensions, morphology, and locations of defects can be captured directly through online monitoring without any destruction to the products[261,265]. Such details can act as strong evidence for the subsequent processing optimization (see Fig. 20). Cunningham et al.[19] determined the critical threshold of laser parameters to avoid unfavorable keyholes on the basis of online synchrotron X-ray imaging. Through analyzing the temperature feedbacks of molten pool, a closed-loop system that equipped with adaptive laser control has been built by Renken et al.[266]. It reduces the risk of defect formation through stabilizing the melting process. Furthermore, multi-sensor monitoring should be capable of providing coupled information including image, temperature field, and acoustic data. Those data can provide more detailed insights into the LPBF processing, which will be of great value for both research and industrial applications.

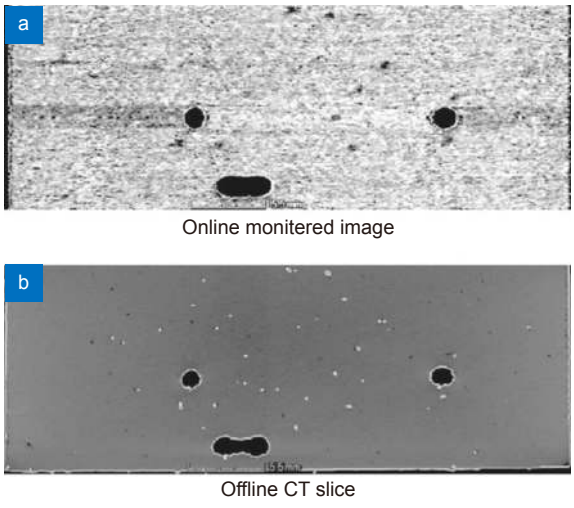

Fig. 20 | Comparison between online monitoring and offline CT images. (**a**) The image acquired through online optical monitoring and (**b**) the offline CT slice at the same layer of a LPBF printed AlSi10Mg sample. Figure reproduced with permission from ref.[265], Springer Nature.

Challenges and potential opportunities

LPBF printed metals are now serving in diverse industries[16]. As a rapid-growing technology, LPBF has its fair

share of scientific and technological challenges. The mechanical performance of LPBF printed metals can be significantly influenced by porosity. Challenges on the evaluation and suppression of porosity stem from the limitations in evaluation methods and the complex laser–matter interactions during LPBF processing. On the other hand, opportunities exist at where the obstacles located. Potential solutions that may be helpful are provided in the following contents. Key concepts of this section are summarized in Fig. 21.

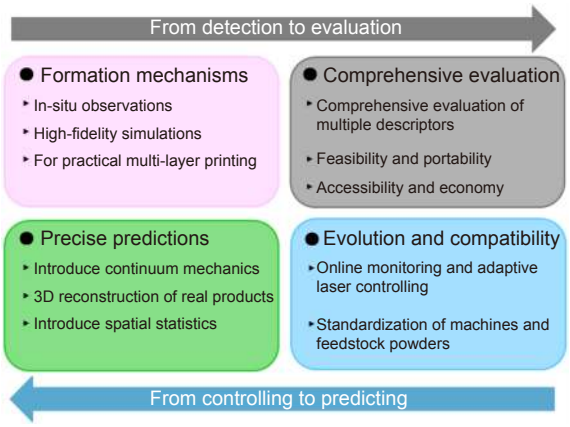

Fig. 21 | Challenges and potential opportunities for the study of porosity in LPBF printed metals.

Formation mechanisms of porosity in multi-layer printing

Great developments have been made in understanding the formation of porosity in single-track printing. A clear formation process of gas porosity has been revealed using in-situ synchrotron X-ray imaging[29]. High-fidelity FEM simulations of single melting track have been performed based on the synchrotron X-ray observations[28]. However, the track-by-track, layer-by-layer LPBF printing generates complicated thermal cycles, resulting in a thermal history that definitely differs from that of single-track investigations. The formation mechanisms of porosity in practical multi-layer printing have not yet been well-studied. This challenge may be addressed in the future using evolved instruments and FEM codes/models. Establishing a database of LPBF-printable metals shall accelerate the research progress on this issue, since physical properties of materials are indispensable for numerical studies. The sensitivities to porosity of various metals can also be included in this database, which will be helpful to avoid the expensive trial-and-error testing in designing processing parameters.

Comprehensive and accessible evaluation of porosity

The merits and drawbacks of currently-available porosity evaluation methods are conspicuous as discussed in above sections. NDE methods lack the ability of precisely measuring the dimensions or the small-scale features of porosity, while DE methods are time-consuming, costly, and even unacceptable in industrial applications. The CT method has been widely used in academia since it can provide 3D reconstructions of porosity, whereas, the dimensions of samples have been strictly limited (generally in millimeter scale) by the flux of X-ray as well as the samples' density. Besides, the inferior portability of CT scanners is a major drawback for industrial applications. Therefore, a comprehensive evaluation method with 3D measuring ability, good accuracy, and reasonable portability can raise a revolution in the evaluation of porosity. The online monitoring appears to be a promising approach since it is capable of providing images of every layer, even every scanning track, without additional time-consumption or any destruction to the products. 3D reconstruction through stacking those online-captured images is technically feasible. Furthermore, a multi-sensor online monitoring system should be able to provide graphical information coupled with thermal data, which is valuable for the in-depth investigation of porosity formation.

Precise prediction of the mechanical performance of LPBF printed metals

As displayed in this review, the majority of predictive models on mechanical properties are staying at the phenomenological stage presently. However, the models based on continuum mechanics have shown ability of predicting the mechanical behaviors of isotropic materials with internal porosity[146]. This technique may be able to be extended to the LPBF printed metals. The actually-detected porosity can be incorporated into the 3D-reconstructed models as the base of FEM meshes. Therefore, high-fidelity simulations of mechanical tests can be performed with the assistance of modern porosity evaluation tools (e.g. micro-CT). In addition, the spatial statistics should be introduced into the product qualification. The influences of porosity is closely-related to its spatial distribution. Clustered and near-surface porosity can be given "more weight" in a spatially-related risk model.

Evolution and compatibility of machines and feedstock powders

Monitoring and adaptive control of laser processes have been successfully implemented in laser cladding, direct energy deposition, and other manufacturing technologies[263]. On the basis of real-time feedbacks, laser parameters are adaptively controlled during processing to achieve better products. A closed-loop, in-process intervention system can eliminate the defects automatically during LPBF processing, improving the quality and repeatability of products. This technology seems promising to be implemented to LPBF since a simple laser remelting can remove most of the porosity within a layer[267]. LPBF machines equipped with a porosity controlling system will be favored by the materials that not suitable for HIP treatment (e.g. 316L and AlSi10Mg). Furthermore, standards for qualifying the as-printed products are developing rapidly owing to the efforts of many organizations such as the ASTM[268]. The development of standards for machines and feedstock powders, however, is relatively sluggish. Significant influences of feedstock powder on the quality of as-printed products have been well-established[24]. Moreover, useful porosity-controlling techniques, such as the "skywriting", have been developed by the manufacturers of LPBF machines but not yet been standardized[269]. Establishment of machine and feedstock standards will be of profound significance to the compatibility and repeatability of LPBF printed metals.

Concluding remarks

The rapid-expanding applications of LPBF printed metals demand for high-performance yet reliable products. As the most universal defect in LPBF printed metals, porosity plays a critical role in determining the mechanical performance and reliability of printed products. A systematic review on the formation, evaluation, effects on mechanical performance, and controlling methods of porosity has been presented in this work. The achievements and challenges have been critically reviewed, with a statistical analysis on the correlation between porosity fraction and tensile properties of four representative metals. This review attempts to provide an overview of the studies focused on the porosity in LPBF printed metals along with potential opportunities for future researches.

Porosity generates primarily from the complicated laser–matter interactions during LPBF processing. The instabilities in molten pool can induce residual gas pores after solidification. The LOF induced by inappropriate processing parameters, spatter shadowing, and other mechanisms can also generate porosity in as-printed metals. The formation mechanisms of single-track printing have been well-established on the basis of in-situ imaging and advanced FEM simulations, whereas, the porosity generated during multi-layer printing has not yet been illustrated clearly.

NDE and DE methods have been extensively employed in the evaluation of porosity. Projected area, AR, and sphericity have been used as common descriptors to evaluate the porosity. NDE methods (e.g. the Archimedes method) can provide an accurate overall quantity of porosity. The resolution of NDE imaging, however, is highly-dependent on the dimensions of samples and the performance of instruments. DE methods hold an intrinsic advantage of providing precise details on the morphology and spatial distribution of porosity, although the applications of DE methods are hindered by their destructive nature. Statistical techniques (e.g. the EVS) have exhibited a good ability in enhancing the generality of limited measurements. Incorporating the spatial information of porosity into evaluation may be a substantial improvement for future studies.

The presence of porosity is detrimental to the mechanical performance of LPBF printed metals, particularly to the tensile properties and fatigue performance. Large and irregular pores are severe stress raisers that facilitate the initiation and propagation of cracks. Statistical analysis in this review shows ductility is most sensitive to porosity among several key tensile properties. The critical limit of porosity fraction before drastic performance degradation is also closely related to ductility. Ductile metals such as 316L SS can sustain apparently higher porosity fractions than the brittle metals such as AlSi10Mg. Thermal expansion of entrapped gas in porosity demands extra attention during post treatments. High-temperature and long-time HTs may induce hazardous porosity growth in less-stiff materials.

Processing optimization is currently the most feasible way to control the porosity in LPBF printed metals. Post HTs with applied pressure are able to further minimize the porosity to a near-zero level. However, HTs are not omnipotent due to the microstructural changes and porosity growth that may happen at elevated temperatures. Online monitoring instruments have been

implemented to assist the in-depth LPBF processing optimization. On the basis of online monitoring and adaptive laser control, automatic defect suppression through in-process intervention can emerge in the near future.

Further study on the formation mechanisms of porosity is requesting for advanced monitoring instruments and high-fidelity simulations. On the other hand, developing NDE methods with excellent detectivity and portability are crucial for the porosity evaluation in LPBF printed metal products. 3D reconstruction based on the online monitoring images may be a promising solution. Semi-empirical models incorporated with continuum mechanics and spatial statics should be of great value in predicting the mechanical performance of LPBF printed metal products. The standardization of machines and feedstocks can further improve the repeatability and reliability.

In summary, studies on the porosity in LPBF printed metals are essential for improving mechanical performance and reliability. Understanding the formation and effects of porosity is an important step to the complete understanding of process-structure-property relationship. Quantitative investigations are requested by the prediction and simulation of mechanical behaviors. With the development of physical theories and models, the formation of porosity can probably be controlled accurately using evolved equipment in the future. The porosity in LPBF printed metals may even be utilized deliberately to achieve specific functions.

References

1. Gibson I, Rosen DW, Stucker B. *Additive Manufacturing Technologies* (Springer, Berlin, 2015).
2. Calignano F, Manfredi D, Ambrosio EP, Biamino S, Lombardi M et al. Overview on additive manufacturing technologies. *Proc IEEE* **105**, 593–612 (2017).
3. Lu BH, Lan HB, Liu HZ. Additive manufacturing frontier: 3D printing electronics. *Opto-Electron Adv* **1**, 170004 (2018).
4. Brighenti R, Cosma MP, Marsavina L, Spagnoli A, Terzano M. Laser-based additively manufactured polymers: a review on processes and mechanical models. *J Mater Sci* **56**, 961–998 (2021).
5. Zhou YH, Li WP, Wang DW, Zhang L, Ohara K et al. Selective laser melting enabled additive manufacturing of Ti–22Al–25Nb intermetallic: excellent combination of strength and ductility, and unique microstructural features associated. *Acta Mater* **173**, 117–129 (2019).
6. Hu YB, Cong WL. A review on laser deposition-additive manufacturing of ceramics and ceramic reinforced metal matrix composites. *Ceram Int* **44**, 20599–20612 (2018).
7. Chueh YH, Zhang XJ, Wei C, Sun Z, Li L. Additive manufacturing of polymer-metal/ceramic functionally graded composite components via multiple material laser powder bed fusion. *J Manuf Sci Eng* **142**, 051003 (2020).
8. Lewandowski JJ, Seifi M. Metal additive manufacturing: a review of mechanical properties. *Annu Rev Mater Res* **46**, 151–186 (2016).
9. ISO/ASTM52900–15 Standard terminology for additive manufacturing – general principles – terminology. *ASTM International*,doi: 10.1520/ISOASTM52900-15 (2015).
10. Xie WD, Mu XX, Guo YX, et al. Research progress of additive manufacturing of high-performance polymers and the applications. *Opto-Electron Eng* **48**, 210137 (2021).
11. Gebhardt A. *Understanding Additive Manufacturing*. Gebhardt A, ed. *Understanding Additive Manufacturing*, edn, (Hanser, Munich, Germany, 2011); https://doi.org/10.3139/9783446431621.fm.
12. Kang JW, Shangguan HL, Deng CY, Hu YY, Yi JH et al. Additive manufacturing-driven mold design for castings. *Addit Manuf* **22**, 472–478 (2018).
13. Hirt L, Reiser A, Spolenak R, Zambelli T. Additive manufacturing of metal structures at the micrometer scale. *Adv Mater* **29**, 1604211 (2017).
14. Herzog D, Seyda V, Wycisk E, Emmelmann C. Additive manufacturing of metals. *Acta Mater* **117**, 371–392 (2016).
15. DebRoy T, Wei HL, Zuback JS, Mukherjee T, Elmer JW et al. Additive manufacturing of metallic components – Process, structure and properties. *Prog Mater Sci* **92**, 112–224 (2018).
16. DebRoy T, Mukherjee T, Milewski JO, Elmer JW, Ribic B et al. Scientific, technological and economic issues in metal printing and their solutions. *Nat Mater* **18**, 1026–1032 (2019).
17. Zhao XY, Deng WW. Printing photovoltaics by electrospray. *Opto-Electron Adv* **3**, 190038 (2020).
18. Haghdadi N, Laleh M, Moyle M, Primig S. Additive manufacturing of steels: a review of achievements and challenges. *J Mater Sci* **56**, 64–107 (2021).
19. Cunningham R, Zhao C, Parab N, Kantzos C, Pauza J et al. Keyhole threshold and morphology in laser melting revealed by ultrahigh-speed x-ray imaging. *Science* **363**, 849–852 (2019).
20. Opatová K, Zetková I, Kučerová L. Relationship between the size and inner structure of particles of virgin and re-used MS1 maraging steel powder for additive manufacturing. *Materials* **13**, 956 (2020).
21. Bartlett JL, Li XD. An overview of residual stresses in metal powder bed fusion. *Addit Manuf* **27**, 131–149 (2019).
22. Kruth JP, Levy G, Klocke F, Childs THC. Consolidation phenomena in laser and powder-bed based layered manufacturing. *CIRP Ann* **56**, 730–759 (2007).
23. Yap CY, Chua CK, Dong ZL, Liu ZH, Zhang DQ et al. Review of selective laser melting: materials and applications. *Appl Phys Rev* **2**, 041101 (2015).
24. Tan JH, Wong WLE, Dalgarno KW. An overview of powder granulometry on feedstock and part performance in the selective laser melting process. *Addit Manuf* **18**, 228–255 (2017).
25. Dong YP, Tang JC, Wang DW, Wang N, He ZD et al. Additive manufacturing of pure Ti with superior mechanical performance, low cost, and biocompatibility for potential replacement of Ti-6Al-4V. *Mater Design* **196**, 109142 (2020).
26. Wang JC, Liu YJ, Qin P, Liang SX, Sercombe TB et al. Selective laser melting of Ti–35Nb composite from elemental powder mixture: microstructure, mechanical behavior and corrosion

behavior. *Mater Sci Eng:A* **760**, 214–224 (2019).
27. Khairallah SA, Anderson AT, Rubenchik A, King WE. Laser powder-bed fusion additive manufacturing: Physics of complex melt flow and formation mechanisms of pores, spatter, and denudation zones. *Acta Mater* **108**, 36–45 (2016).
28. Khairallah SA, Martin AA, Lee JRI, Guss G, Calta NP et al. Controlling interdependent meso-nanosecond dynamics and defect generation in metal 3D printing. *Science* **368**, 660–665 (2020).
29. Zhao C, Parab ND, Li XX, Fezzaa K, Tan WD et al. Critical instability at moving keyhole tip generates porosity in laser melting. *Science* **370**, 1080–1086 (2020).
30. Zhang B, Li YT, Bai Q. Defect formation mechanisms in selective laser melting: a review. *Chin J Mech Eng* **30**, 515–527 (2017).
31. Taheri H, Shoaib MRBM, Koester LW, Bigelow TA, Collins PC et al. Powder-based additive manufacturing - a review of types of defects, generation mechanisms, detection, property evaluation and metrology. *Int J Addit Subtract Mater Manuf* **1**, 172–209 (2017).
32. Gu DD, Hagedorn YC, Meiners W, Meng GB, Batista RJS et al. Densification behavior, microstructure evolution, and wear performance of selective laser melting processed commercially pure titanium. *Acta Mater* **60**, 3849–3860 (2012).
33. Bidare P, Bitharas I, Ward RM, Attallah MM, Moore AJ. Fluid and particle dynamics in laser powder bed fusion. *Acta Mater* **142**, 107–120 (2018).
34. Ye JC, Khairallah SA, Rubenchik AM, Crumb MF, Guss G et al. Energy coupling mechanisms and scaling behavior associated with laser powder bed fusion additive manufacturing. *Adv Eng Mater* **21**, 1900185 (2019).
35. Tenbrock C, Kelliger T, Praetzsch N, Ronge M, Jauer L et al. Effect of laser-plume interaction on part quality in multi-scanner Laser Powder Bed Fusion. *Addit Manuf* **38**, 101810 (2021).
36. Xie XZ, Zhou CX, Wei X, Hu W, Ren QL. Laser machining of transparent brittle materials: from machining strategies to applications. *Opto-Electron Adv* **2**, 180017 (2019).
37. Wang DW, Zhou YH, Shen J, Liu Y, Li DF et al. Selective laser melting under the reactive atmosphere: a convenient and efficient approach to fabricate ultrahigh strength commercially pure titanium without sacrificing ductility. *Mater Sci Eng:A* **762**, 138078 (2019).
38. Sanaei N, Fatemi A. Defects in additive manufactured metals and their effect on fatigue performance: a state-of-the-art review. *Prog Mater Sci* **117**, 100724 (2021).
39. Leung CLA, Marussi S, Atwood RC, Towrie M, Withers PJ et al. In situ X-ray imaging of defect and molten pool dynamics in laser additive manufacturing. *Nat Commun* **9**, 1355 (2018).
40. Du Plessis A, Yadroitsava I, Yadroitsev I. Effects of defects on mechanical properties in metal additive manufacturing: a review focusing on X-ray tomography insights. *Mater Design* **187**, 108385 (2020).
41. Pineau A, Benzerga AA, Pardoen T. Failure of metals I: brittle and ductile fracture. *Acta Mater* **107**, 424–483 (2016).
42. Ng GKL, Jarfors AEW, Bi G, Zheng HY. Porosity formation and gas bubble retention in laser metal deposition. *Appl Phys A* **97**, 641–649 (2009).
43. Kasperovich G, Haubrich J, Gussone J, Requena G. Correlation between porosity and processing parameters in TiAl6V4 produced by selective laser melting. *Mater Design* **105**, 160–170 (2016).
44. Zhou X, Wang DZ, Liu XH, Zhang DD, Qu SL et al. 3D-imaging of selective laser melting defects in a Co–Cr–Mo alloy by synchrotron radiation micro-CT. *Acta Mater* **98**, 1–16 (2015).
45. Leuders S, Thöne M, Riemer A, Niendorf T, Tröster T et al. On the mechanical behaviour of titanium alloy TiAl6V4 manufactured by selective laser melting: fatigue resistance and crack growth performance. *Int J Fatigue* **48**, 300–307 (2013).
46. Zhao B, Gain AK, Ding WF, Zhang LC, Li XY et al. A review on metallic porous materials: pore formation, mechanical properties, and their applications. *Int J Adv Manuf Technol* **95**, 2641–2659 (2018).
47. Tammas-Williams S, Withers PJ, Todd I, Prangnell PB. Porosity regrowth during heat treatment of hot isostatically pressed additively manufactured titanium components. *Scr Mater* **122**, 72–76 (2016).
48. Girelli L, Tocci M, Gelfi M, Pola A. Study of heat treatment parameters for additively manufactured AlSi10Mg in comparison with corresponding cast alloy. *Mater Sci Eng:A* **739**, 317–328 (2019).
49. Barua S, Liou F, Newkirk J, Sparks T. Vision-based defect detection in laser metal deposition process. *Rapid Prototyping J* **20**, 77–85 (2014).
50. Hojjatzadeh SMH, Parab ND, Yan WT, Guo QL, Xiong LH et al. Pore elimination mechanisms during 3D printing of metals. *Nat Commun* **10**, 3088 (2019).
51. King WE, Barth HD, Castillo VM, Gallegos GF, Gibbs JW et al. Observation of keyhole-mode laser melting in laser powder-bed fusion additive manufacturing. *J Mater Process Technol* **214**, 2915–2925 (2014).
52. Ge WJ, Fuh JYH, Na SJ. Numerical modelling of keyhole formation in selective laser melting of Ti6Al4V. *J Manuf Process* **62**, 646–654 (2021).
53. Wang L, Zhang YM, Yan WT. Evaporation model for keyhole dynamics during additive manufacturing of metal. *Phys Rev Appl* **14**, 064039 (2020).
54. Zhao C, Guo QL, Li XX, Parab N, Fezzaa K et al. Bulk-explosion-induced metal spattering during laser processing. *Phys Rev X* **9**, 021052 (2019).
55. Anisimov SI, Khokhlov VA. *Instabilities in Laser-Matter Interaction*. (CRC Press, Boca Raton, 1995).
56. Sankin GN, Simmons WN, Zhu SL, Zhong P. Shock wave interaction with laser-generated single bubbles. *Phys Rev Lett* **95**, 034501 (2005).
57. Tang M, Pistorius PC. Oxides, porosity and fatigue performance of AlSi10Mg parts produced by selective laser melting. *Int J Fatigue* **94**, 192–201 (2017).
58. Weingarten C, Buchbinder D, Pirch N, Meiners W, Wissenbach K et al. Formation and reduction of hydrogen porosity during selective laser melting of AlSi10Mg. *J Mater Process Technol* **221**, 112–120 (2015).
59. Zeng GH, Song T, Dai YH, Tang HP, Yan M. 3D printed breathable mould steel: small micrometer-sized, interconnected pores by creatively introducing foaming agent to additive manufacturing. *Mater Design* **169**, 107693 (2019).
60. Chen G, Zhao SY, Tan P, Wang J, Xiang CS et al. A comparative study of Ti-6Al-4V powders for additive manufacturing by gas atomization, plasma rotating electrode process and

plasma atomization. *Powder Technol* **333**, 38–46 (2018).
61. Chen G, Zhou Q, Zhao SY, Yin JO, Tan P et al. A pore morphological study of gas-atomized Ti-6Al-4V powders by scanning electron microscopy and synchrotron X-ray computed tomography. *Powder Technol* **330**, 425–430 (2018).
62. Ternovoi YF, Tsipunov AG, Kuratchenko SB, Kuimova OM, Kondakova KV. Pore formation in atomized powders. *Sov Powder Metall Met Ceram* **24**, 10–13 (1985).
63. Tammas-Williams S, Zhao H, Léonard F, Derguti F, Todd I et al. XCT analysis of the influence of melt strategies on defect population in Ti–6Al–4V components manufactured by Selective Electron Beam Melting. *Mater Characteriz* **102**, 47–61 (2015).
64. Wu ZH, Basu D, Meyer JLL, Larson E, Kuo R et al. Study of powder gas entrapment and its effects on porosity in 17-4 PH stainless steel parts fabricated in laser powder bed fusion. *JOM* **73**, 177–188 (2021).
65. Li S, Hassanin H, Attallah MM, Adkins NJE, Essa K. The development of TiNi-based negative Poisson's ratio structure using selective laser melting. *Acta Mater* **105**, 75–83 (2016).
66. Cunningham R, Nicolas A, Madsen J, Fodran E, Anagnostou E et al. Analyzing the effects of powder and post-processing on porosity and properties of electron beam melted Ti-6Al-4V. *Mater Res Lett* **5**, 516–525 (2017).
67. Braun J, Kaserer L, Stajkovic J, Leitz KH, Tabernig B et al. Molybdenum and tungsten manufactured by selective laser melting: analysis of defect structure and solidification mechanisms. *Int J Refract Met Hard Mater* **84**, 104999 (2019).
68. Polozov I, Sufiiarov V, Kantyukov A, Popovich A. Selective Laser Melting of Ti_2AlNb-based intermetallic alloy using elemental powders: effect of process parameters and post-treatment on microstructure, composition, and properties. *Intermetallics* **112**, 106554 (2019).
69. Tang M, Pistorius PC, Beuth JL. Prediction of lack-of-fusion porosity for powder bed fusion. *Addit Manuf* **14**, 39–48 (2017).
70. Chlebus E, Kuźnicka B, Kurzynowski T, Dybała B. Microstructure and mechanical behaviour of Ti—6Al—7Nb alloy produced by selective laser melting. *Mater Characteriz* **62**, 488–495 (2011).
71. Attar H, Löber L, Funk A, Calin M, Zhang LC et al. Mechanical behavior of porous commercially pure Ti and Ti–TiB composite materials manufactured by selective laser melting. *Mater Sci Eng:A* **625**, 350–356 (2015).
72. Hou YH, Liu B, Liu Y, Zhou YH, Song TT et al. Ultra-low cost Ti powder for selective laser melting additive manufacturing and superior mechanical properties associated. *Opto-Electron Adv* **2**, 180028 (2019).
73. Honarvar F, Varvani-Farahani A. A review of ultrasonic testing applications in additive manufacturing: defect evaluation, material characterization, and process control. *Ultrasonics* **108**, 106227 (2020).
74. Waller JM, Parker BH, Hodges KL, Burke ER, Walker JL et al. Nondestructive evaluation of additive manufacturing. National Aeronautics and Space Administration, (2014).
75. Masuo H, Tanaka Y, Morokoshi S, Yagura H, Uchida T et al. Effects of defects, surface roughness and HIP on fatigue strength of Ti-6Al-4V manufactured by additive manufacturing. *Proced Struct Integrity* **7**, 19–26 (2017).
76. Wits WW, Carmignato S, Zanini F, Vaneker THJ. Porosity testing methods for the quality assessment of selective laser melted parts. *CIRP Ann* **65**, 201–204 (2016).
77. Rafi HK, Karthik NV, Gong HJ, Starr TL, Stucker BE. Microstructures and mechanical properties of Ti6Al4V parts fabricated by selective laser melting and electron beam melting. *J Mater Eng Perform* **22**, 3872–3883 (2013).
78. Slotwinski JA, Garboczi EJ. Porosity of additive manufacturing parts for process monitoring. *AIP Conf Proc* **1581**, 1197–1204 (2014).
79. Monchiet V, Bonnet G. A gurson-type model accounting for void size effects. *Int J Solids Struct* **50**, 320–327 (2013).
80. Becker R. The effect of porosity distribution on ductile failure. *J Mech Phys Solids* **35**, 577–599 (1987).
81. Romano S, Abel A, Gumpinger J, Brandão AD, Beretta S. Quality control of AlSi10Mg produced by SLM: metallography versus CT scans for critical defect size assessment. *Addit Manuf* **28**, 394–405 (2019).
82. Romano S, Brandão A, Gumpinger J, Gschweitl M, Beretta S. Qualification of AM parts: extreme value statistics applied to tomographic measurements. *Mater Design* **131**, 32–48 (2017).
83. Murakami Y. Effects of small defects and nonmetallic inclusions on the fatigue strength of metals. *JSME Int J Ser I, Solid Mech Strength Mater* **32**, 167–180 (1989).
84. Sanaei N, Fatemi A, Phan N. Defect characteristics and analysis of their variability in metal L-PBF additive manufacturing. *Mater Design* **182**, 108091 (2019).
85. Romano S, Brückner-Foit A, Brandão A, Gumpinger J, Ghidini T et al. Fatigue properties of AlSi10Mg obtained by additive manufacturing: defect-based modelling and prediction of fatigue strength. *Eng Fract Mech* **187**, 165–189 (2018).
86. Murakami Y, Beretta S. Small defects and inhomogeneities in fatigue strength: experiments, models and statistical implications. *Extremes* **2**, 123–147 (1999).
87. Pineau A, McDowell DL, Busso EP, Antolovich SD. Failure of metals II: fatigue. *Acta Mater* **107**, 484–507 (2016).
88. Murakami Y. Inclusion rating by statistics of extreme values and its application to fatigue strength prediction and quality control of materials. *J Res Natl Inst Stand Technol* **99**, 345–351 (1994).
89. Dowling NE, Katakam S, Narayanasamy R. *Mechanical Behavior of Materials: Engineering Methods for Deformation, Fracture, and Fatigue* (Pearson Education Limited, London, 2012).
90. Kabir MR, Richter H. Modeling of processing-induced pore morphology in an additively-manufactured Ti-6Al-4V alloy. *Materials* **10**, 145 (2017).
91. Mbiakop A, Constantinescu A, Danas K. An analytical model for porous single crystals with ellipsoidal voids. *J Mech Phys Solids* **84**, 436–467 (2015).
92. Madou K, Leblond JB, Morin L. Numerical studies of porous ductile materials containing arbitrary ellipsoidal voids – II: Evolution of the length and orientation of the void axes. *Eur J Mech - A/Solid* **42**, 490–507 (2013).
93. Komori K. Improvement of an ellipsoidal void model for simulating ductile fracture behavior. *Key Eng Mater* **577 –578**, 93–96 (2013).
94. Komori K. An ellipsoidal void model for simulating ductile fracture behavior. *Mech Mater* **60**, 36–54 (2013).
95. Hidetaka K. What did archimedes find at “Eureka” moment?. Paipetis SA, Ceccarelli M, eds. *The Genius of Archimedes* --

23 Centuries of Influence on Mathematics, Science and Engineering, 265–276 (Springer, Dordrecht, 2010).

96. Spierings AB, Schneider M, Eggenberger R. Comparison of density measurement techniques for additive manufactured metallic parts. *Rapid Prototyping J* **17**, 380–386 (2011).
97. Kasperovich G, Hausmann J. Improvement of fatigue resistance and ductility of TiAl6V4 processed by selective laser melting. *J Mater Process Technol* **220**, 202–214 (2015).
98. Chen P, Li S, Zhou YH, Yan M, Attallah MM. Fabricating CoCrFeMnNi high entropy alloy via selective laser melting in-situ alloying. *J Mater Sci Technol* **43**, 40–43 (2020).
99. Taylor RP, McClain ST, Berry JT. Uncertainty analysis of metal-casting porosity measurements using Archimedes' principle. *Int J Cast Met Res* **11**, 247–257 (1999).
100. Kak AC, Slaney M, Wang G. Principles of computerized tomographic imaging. *Med Phys* **29**, 107 (2002).
101. Cunningham R, Narra SP, Montgomery C, Beuth J, Rollett AD. Synchrotron-based X-ray microtomography characterization of the effect of processing variables on porosity formation in laser power-bed additive manufacturing of Ti-6Al-4V. *JOM* **69**, 479–484 (2017).
102. Kantzos CA, Cunningham RW, Tari V, Rollett AD. Characterization of metal additive manufacturing surfaces using synchrotron X-ray CT and micromechanical modeling. *Comput Mech* **61**, 575–580 (2018).
103. Abd Halim S, Abd Halim MS, Hadi NA. Surface Reconstruction from Computed Tomography (CT) Image of Human Head with the Effect of Noise. *AIP Conf Proc* **2013**, 020017 (2018).
104. Ziółkowski G, Chlebus E, Szymczyk P, Kurzac J. Application of X-ray CT method for discontinuity and porosity detection in 316L stainless steel parts produced with SLM technology. *Arch Civ Mech Eng* **14**, 608–614 (2014).
105. Gong H, Rafi K, Starr T, Stucker B. c. In *Proceedings of the 24th Annual International Solid Freeform Fabrication Symposium—An Additive Manufacturing Conference* 12–14 (2013).
106. Vanderesse N, Ky I, González FQ, Nuño N, Bocher P. Image analysis characterization of periodic porous materials produced by additive manufacturing. *Mater Design* **92**, 767–778 (2016).
107. Xia MJ, Gu DD, Yu GQ, Dai DH, Chen HY et al. Porosity evolution and its thermodynamic mechanism of randomly packed powder-bed during selective laser melting of Inconel 718 alloy. *Int J Mach Tools Manu* **116**, 96–106 (2017).
108. Attar H, Ehtemam-Haghighi S, Kent D, Wu XH, Dargusch MS. Comparative study of commercially pure titanium produced by laser engineered net shaping, selective laser melting and casting processes. *Mater Sci Eng:A* **705**, 385–393 (2017).
109. Cheeke JDN. *Fundamentals and Applications of Ultrasonic Waves* (CRC Press, Boca Raton, 2010).
110. Shull PJ. *Nondestructive Evaluation: Theory, Techniques, and Applications* (Marcel Dekker, New York, 2002).
111. Fathi-Haftshejani P, Honarvar F. Nondestructive evaluation of clad rods by inversion of acoustic scattering data. *J Nondestruct Eval* **38**, 67 (2019).
112. Everton SK, Dickens P, Tuck C, Dutton B. Identification of subsurface defects in parts produced by additive manufacturing, using laser generated ultrasound. Additive Manufacturing and 3D Printing Research Group, University of Nottingham, (2016).
113. Slotwinski JA, Garboczi EJ, Hebenstreit KM. Porosity measurements and analysis for metal additive manufacturing process control. *J Res Natl Inst Stand Technol* **119**, 494–528 (2014).
114. Cerniglia D, Scafidi M, Pantano A, Rudlin J. Inspection of additive-manufactured layered components. *Ultrasonics* **62**, 292–298 (2015).
115. Nadimpalli VK, Yang L, Nagy PB. In-situ interfacial quality assessment of Ultrasonic Additive Manufacturing components using ultrasonic NDE. *NDT E Int* **93**, 117–130 (2018).
116. Javadi Y, Mohseni E, MacLeod CN, Lines D, Vasilev M et al. Continuous monitoring of an intentionally-manufactured crack using an automated welding and in-process inspection system. *Mater Design* **191**, 108655 (2020).
117. Wang XH, Li WT, Li Y, Zhou ZG, Zhang JJ et al. Phased array ultrasonic testing of micro-flaws in additive manufactured titanium block. *Mater Res Express* **7**, 016572 (2020).
118. Mahmoudi M, Elwany A, Yadollahi A, Thompson SM, Bian LK et al. Mechanical properties and microstructural characterization of selective laser melted 17-4 PH stainless steel. *Rapid Prototyping J* **23**, 280–294 (2017).
119. Vilardell AM, Fredriksson G, Yadroitsev I, Krakhmalev P. Fracture mechanisms in the as-built and stress-relieved laser powder bed fusion Ti6Al4V ELI alloy. *Opt Laser Technol* **109**, 608–615 (2019).
120. Su XM. Toward an understanding of local variability of fatigue strength with microstructures. *Int J Fatigue* **30**, 1007–1015 (2008).
121. Geetha M, Singh AK, Asokamani R, Gogia AK. Ti based biomaterials, the ultimate choice for orthopaedic implants – A review. *Prog Mater Sci* **54**, 397–425 (2009).
122. Luo JP, Huang YJ, Xu JY, Sun JF, Dargusch MS et al. Additively manufactured biomedical Ti-Nb-Ta-Zr lattices with tunable Young's modulus: mechanical property, biocompatibility, and proteomics analysis. *Mater Sci Eng:C* **114**, 110903 (2020).
123. Gong HJ, Rafi K, Gu HF, Ram GDJ, Starr T et al. Influence of defects on mechanical properties of Ti–6Al–4 V components produced by selective laser melting and electron beam melting. *Mater Design* **86**, 545–554 (2015).
124. Waddell M, Walker K, Bandyopadhyay R, Kapoor K, Mallory A et al. Small fatigue crack growth behavior of Ti-6Al-4V produced via selective laser melting: in situ characterization of a 3D crack tip interactions with defects. *Int J Fatigue* **137**, 105638 (2020).
125. Aqida SN, Ghazali MI, Hashim J. Effect of porosity on mechanical properties of metal matrix composite: an overview. *Jurnal Teknologi* **40**, 17–32 (2004).
126. Hardin RA, Beckermann C. Effect of porosity on the stiffness of cast steel. *Metall Mater Trans A* **38**, 2992–3006 (2007).
127. Schijve J. Stress concentration at notches. Schijve J, ed. *Fatigue of Structures and Materials*, 45–70 (Springer, Dordrecht, 2001).
128. Bert CW. Prediction of elastic moduli of solids with oriented porosity. *J Mater Sci* **20**, 2220–2224 (1985).
129. Rossi RC. Prediction of the elastic moduli of composites. *J Am Ceram Soc* **51**, 433–440 (1968).
130. Roberts AP, Garboczi EJ. Elastic properties of model porous ceramics. *J Am Ceram Soc* **83**, 3041–3048 (2000).
131. Zhang EL, Wang B. On the compressive behaviour of sintered porous coppers with low to medium porosities —Part I:

experimental study. *Int J Mech Sci* **47**, 744–756 (2005).
132. Gibson LJ, Ashby MF. *Cellular Solids: Structure and Properties* 2nd ed (Cambridge University Press, Cambridge, 1997).
133. Tekmen C, Ozdemir I, Cocen U, Onel K. The mechanical response of Al–Si–Mg/SiC_p composite: influence of porosity. *Mater Sci Eng:A* **360**, 365–371 (2003).
134. Palchik V, Hatzor YH. The influence of porosity on tensile and compressive strength of porous chalks. *Rock Mech Rock Eng* **37**, 331–341 (2004).
135. Lecarme L, Tekoğlu C, Pardoen T. Void growth and coalescence in ductile solids with stage III and stage IV strain hardening. *Int J Plast* **27**, 1203–1223 (2011).
136. Feng ZQ, Yang YQ, Chen YX, Huang B, Fu MS et al. In-situ TEM investigation of fracture process in an Al–Cu–Mg alloy. *Mater Sci Eng:A* **586**, 259–266 (2013).
137. Ragab AR. A model for ductile fracture based on internal necking of spheroidal voids. *Acta Mater* **52**, 3997–4009 (2004).
138. Yadroitsev I, Krakhmalev P, Yadroitsava I, Du Plessis A. Qualification of Ti6Al4V ELI alloy produced by laser powder bed fusion for biomedical applications. *JOM* **70**, 372–377 (2018).
139. Rollett AD, Kocks UF. A review of the stages of work hardening. *Solid State Phenom* **35–36**, 1–18 (1993).
140. Susmel L, Taylor D. On the use of the theory of critical distances to predict static failures in ductile metallic materials containing different geometrical features. *Eng Fract Mech* **75**, 4410–4421 (2008).
141. Voisin T, Calta NP, Khairallah SA, Forien JB, Balogh L et al. Defects-dictated tensile properties of selective laser melted Ti-6Al-4V. *Mater Design* **158**, 113–126 (2018).
142. Benzerga AA, Besson J, Pineau A. Anisotropic ductile fracture: Part I: experiments. *Acta Mater* **52**, 4623–4638 (2004).
143. Gurson AL. Continuum theory of ductile rupture by void nucleation and growth: Part I—yield criteria and flow rules for porous ductile media. *J Eng Mater Technol* **99**, 2–15 (1977).
144. Tvergaard V. On localization in ductile materials containing spherical voids. *Int J Fract* **18**, 237–252 (1982).
145. Needleman A. A continuum model for void nucleation by inclusion debonding. *J Appl Mech Sep* **54**, 525–531 (1987).
146. Hao S, Brocks W. The Gurson-Tvergaard-Needleman-model for rate and temperature-dependent materials with isotropic and kinematic hardening. *Comput Mech* **20**, 34–40 (1997).
147. Haynes R. A study of the effect of porosity content on the ductility of sintered metals. *Powder Metal* **20**, 17–20 (1977).
148. Yadollahi A, Shamsaei N. Additive manufacturing of fatigue resistant materials: challenges and opportunities. *Int J Fatigue* **98**, 14–31 (2017).
149. Daniewicz SR, Shamsaei N. An introduction to the fatigue and fracture behavior of additive manufactured parts. *Int J Fatigue* **94**, 167 (2017).
150. Tammas-Williams S, Withers PJ, Todd I, Prangnell PB. The influence of porosity on fatigue crack initiation in additively manufactured titanium components. *Sci Rep* **7**, 7308 (2017).
151. Biswal R, Zhang X, Syed AK, Awd M, Ding JL et al. Criticality of porosity defects on the fatigue performance of wire + arc additive manufactured titanium alloy. *Int J Fatigue* **122**, 208–217 (2019).
152. Liao D, Zhu SP, Correia JAFO, De Jesus AMP, Berto F. Recent advances on notch effects in metal fatigue: a review. *Fatigue Fract Eng Mater Struct* **43**, 637–659 (2020).
153. Chastand V, Tezenas A, Cadoret Y, Quaegebeur P, Maia W et al. Fatigue characterization of Titanium Ti-6Al-4V samples produced by additive manufacturing. *Proced Struct Inte* **2**, 3168–3176 (2016).
154. Taylor D. The theory of critical distances. *Eng Fract Mech* **75**, 1696–1705 (2008).
155. Skallerud B, Iveland T, Härkegård G. Fatigue life assessment of aluminum alloys with casting defects. *Eng Fract Mech* **44**, 857–874 (1993).
156. Sheridan L, Scott-Emuakpor OE, George T, Gockel JE. Relating porosity to fatigue failure in additively manufactured alloy 718. *Mater Sci Eng:A* **727**, 170–176 (2018).
157. Yamashita Y, Murakami T, Mihara R, Okada M, Murakami Y. Defect analysis and fatigue design basis for Ni-based superalloy 718 manufactured by selective laser melting. *Int J Fatigue* **117**, 485–495 (2018).
158. Prithivirajan V, Sangid MD. The role of defects and critical pore size analysis in the fatigue response of additively manufactured IN718 via crystal plasticity. *Mater Design* **150**, 139–153 (2018).
159. Murakami Y. *Metal Fatigue: Effects of Small Defects and Nonmetallic Inclusions* 2nd ed (Academic Press, London, 2019).
160. Susmel L. The theory of critical distances: a review of its applications in fatigue. *Eng Fract Mech* **75**, 1706–1724 (2008).
161. Taylor D. Applications of the theory of critical distances in failure analysis. *Eng Fail Anal* **18**, 543–549 (2011).
162. Newman JC, Piascik RS. *Fatigue Crack Growth Thresholds, Endurance Limits, and Design* (ASTM International, West Conshohocken, PA, 2000).
163. Witkin DB, Patel DN, Helvajian H, Steffeney L, Diaz A. Surface treatment of powder-bed fusion additive manufactured metals for improved fatigue life. *J Mater Eng Perform* **28**, 681–692 (2019).
164. Fatemi A, Molaei R, Phan N. Multiaxial fatigue of additive manufactured metals. *MATEC Web Conf* **300**, 01003 (2019).
165. Ronneberg T, Davies CM, Hooper PA. Revealing relationships between porosity, microstructure and mechanical properties of laser powder bed fusion 316L stainless steel through heat treatment. *Mater Design* **189**, 108481 (2020).
166. Shipley H, McDonnell D, Culleton M, Coull R, Lupoi R et al. Optimisation of process parameters to address fundamental challenges during selective laser melting of Ti-6Al-4V: a review. *Int J Mach Tools Manuf* **128**, 1–20 (2018).
167. DebRoy T, Mukherjee T, Wei HL, Elmer JW, Milewski JO. Metallurgy, mechanistic models and machine learning in metal printing. *Nat Rev Mater* **6**, 48–68 (2021).
168. Lütjering G, Williams JC. *Titanium* (Springer, Berlin Heidelberg, 2007).
169. Qian M, Xu W, Brandt M, Tang HP. Additive manufacturing and postprocessing of Ti-6Al-4V for superior mechanical properties. *MRS Bull* **41**, 775–784 (2016).
170. Liu SY, Shin YC. Additive manufacturing of Ti6Al4V alloy: a review. *Mater Design* **164**, 107552 (2019).
171. Murr LE, Quinones SA, Gaytan SM, Lopez MI, Rodela A et al. Microstructure and mechanical behavior of Ti–6Al–4V produced by rapid-layer manufacturing, for biomedical applications. *J Mech Behav Biomed Mater* **2**, 20–32 (2009).
172. Thijs L, Verhaeghe F, Craeghs T, Van Humbeeck J, Kruth JP. A study of the microstructural evolution during selective laser

melting of Ti–6Al–4V. *Acta Mater* **58**, 3303–3312 (2010).
173. Krakhmalev P, Fredriksson G, Yadroitsava I, Kazantseva N, Du Plessis A et al. Deformation behavior and microstructure of Ti6Al4V manufactured by SLM. *Phys Proced* **83**, 778–788 (2016).
174. Xu W, Brandt M, Sun S, Elambasseril J, Liu Q et al. Additive manufacturing of strong and ductile Ti–6Al–4V by selective laser melting via in situ martensite decomposition. *Acta Mater* **85**, 74–84 (2015).
175. Losertová M, Kubeš V. Microstructure and mechanical properties of selective laser melted Ti6Al4V alloy. *IOP Conf Ser:Mater Sci Eng* **266**, 012009 (2017).
176. Vilaro T, Colin C, Bartout JD. As-Fabricated and heat-treated microstructures of the Ti-6Al-4V alloy processed by selective laser melting. *Metall Mater Trans A* **42**, 3190–3199 (2011).
177. Mertens A, Reginster S, Paydas H, Contrepois Q, Dormal T et al. Mechanical properties of alloy Ti–6Al–4V and of stainless steel 316L processed by selective laser melting: influence of out-of-equilibrium microstructures. *Powder Metal* **57**, 184–189 (2014).
178. Yan M, Xu W, Dargusch MS, Tang HP, Brandt M et al. Review of effect of oxygen on room temperature ductility of titanium and titanium alloys. *Powder Metal* **57**, 251–257 (2014).
179. Yu Q, Qi L, Tsuru T, Traylor R, Rugg D et al. Origin of dramatic oxygen solute strengthening effect in titanium. *Science* **347**, 635–639 (2015).
180. Facchini L, Magalini E, Robotti P, Molinari A, Höges S et al. Ductility of a Ti-6Al-4V alloy produced by selective laser melting of prealloyed powders. *Rapid Prototyping J* **16**, 450–459 (2010).
181. Wysocki B, Maj P, Sitek R, Buhagiar J, Kurzydłowski KJ et al. Laser and electron beam additive manufacturing methods of fabricating titanium bone implants. *Appl Sci* **7**, 657 (2017).
182. Simonelli M, Tse YY, Tuck C. The formation of α + β microstructure in as-fabricated selective laser melting of Ti–6Al–4V. *J Mater Res* **29**, 2028–2035 (2014).
183. Qiu CL, Adkins NJE, Attallah MM. Microstructure and tensile properties of selectively laser-melted and of HIPed laser-melted Ti–6Al–4V. *Mater Sci Eng:A* **578**, 230–239 (2013).
184. Saravanan M, Devaraju A, Venkateshwaran N, Krishnakumari A, Saarvesh J. A review on recent progress in coatings on AISI austenitic stainless steel. *Mater Today:Proc* **5**, 14392–14396 (2018).
185. Kong DC, Ni XQ, Dong CF, Lei XW, Zhang L et al. Bio-functional and anti-corrosive 3D printing 316L stainless steel fabricated by selective laser melting. *Mater Design* **152**, 88–101 (2018).
186. Wang YM, Voisin T, McKeown JT, Ye JC, Calta NP et al. Additively manufactured hierarchical stainless steels with high strength and ductility. *Nat Mater* **17**, 63–71 (2018).
187. Zhong Y, Liu LF, Wikman S, Cui DQ, Shen ZJ. Intragranular cellular segregation network structure strengthening 316L stainless steel prepared by selective laser melting. *J Nucl Mater* **470**, 170–178 (2016).
188. Saeidi K, Gao X, Lofaj F, Kvetkova L, Shen ZJ. Transformation of austenite to duplex austenite-ferrite assembly in annealed stainless steel 316L consolidated by laser melting. *J Alloys Compd* **633**, 463–469 (2015).
189. Kong DC, Ni XQ, Dong CF, Zhang L, Man C et al. Heat treatment effect on the microstructure and corrosion behavior of 316L stainless steel fabricated by selective laser melting for proton exchange membrane fuel cells. *Electrochim Acta* **276**, 293–303 (2018).
190. Ni XQ, Kong DC, Wen Y, Zhang L, Wu WH et al. Anisotropy in mechanical properties and corrosion resistance of 316L stainless steel fabricated by selective laser melting. *Int J Miner, Metall, Mater* **26**, 319–328 (2019).
191. Kurzynowski T, Gruber K, Stopyra W, Kuźnicka B, Chlebus E. Correlation between process parameters, microstructure and properties of 316 L stainless steel processed by selective laser melting. *Mater Sci Eng:A* **718**, 64–73 (2018).
192. Mertens A, Reginster S, Contrepois Q, Dormal T, Lemaire O et al. Microstructures and mechanical properties of stainless steel aisi 316l processed by selective laser melting. *Mater Sci Forum* **783–786**, 898–903 (2014).
193. Kong DC, Dong CF, Ni XQ, Zhang L, Yao JZ et al. Mechanical properties and corrosion behavior of selective laser melted 316L stainless steel after different heat treatment processes. *J Mater Sci Technol* **35**, 1499–1507 (2019).
194. Stoll P, Spierings A, Wegener K. Impact of a process interruption on tensile properties of SS 316L parts and hybrid parts produced with selective laser melting. *Int J Adv Manuf Technol* **103**, 367–376 (2019).
195. Blinn B, Klein M, Glassner C, Smaga M, Aurich JC et al. An investigation of the microstructure and fatigue behavior of additively manufactured AISI 316L stainless steel with regard to the influence of heat treatment. *Metals* **8**, 220 (2018).
196. Yin YJ, Sun JQ, Guo J, Kan XF, Yang DC. Mechanism of high yield strength and yield ratio of 316 L stainless steel by additive manufacturing. *Mater Sci Eng:A* **744**, 773–777 (2019).
197. Wang GQ, Liu Q, Rao H, Liu HC, Qiu CL. Influence of porosity and microstructure on mechanical and corrosion properties of a selectively laser melted stainless steel. *J Alloys Compd* **831**, 154815 (2020).
198. Jeon JM, Park JM, Yu JH, Kim JG, Seong Y et al. Effects of microstructure and internal defects on mechanical anisotropy and asymmetry of selective laser-melted 316L austenitic stainless steel. *Mater Sci Eng:A* **763**, 138152 (2019).
199. Wu AS, Brown DW, Kumar M, Gallegos GF, King WE. An experimental investigation into additive manufacturing-induced residual stresses in 316L stainless steel. *Metall Mater Trans A* **45**, 6260–6270 (2014).
200. Amato KN, Gaytan SM, Murr LE, Martinez E, Shindo PW et al. Microstructures and mechanical behavior of Inconel 718 fabricated by selective laser melting. *Acta Mater* **60**, 2229–2239 (2012).
201. Hosseini E, Popovich VA. A review of mechanical properties of additively manufactured Inconel 718. *Addit Manuf* **30**, 100877 (2019).
202. Yi JH, Kang JW, Wang TJ, Wang X, Feng T et al. Microstructure and mechanical behavior of bright crescent areas in Inconel 718 sample fabricated by selective laser melting. *Mater Design* **197**, 109259 (2021).
203. Qi H, Azer M, Ritter A. Studies of standard heat treatment effects on microstructure and mechanical properties of laser net shape manufactured INCONEL 718. *Metall Mater Trans A* **40**, 2410–2422 (2009).
204. Paulonis DF, Schirra JJ. Alloy 718 at Pratt & Whitney-Historical

perspective and future challenges. *Superalloys* **718**, 13–23 (2001).
205. Aydinöz ME, Brenne F, Schaper M, Schaak C, Tillmann W et al. On the microstructural and mechanical properties of post-treated additively manufactured Inconel 718 superalloy under quasi-static and cyclic loading. *Mater Sci Eng:A* **669**, 246–258 (2016).
206. Kirka MM, Unocic KA, Raghavan N, Medina F, Dehoff RR et al. Microstructure development in electron beam-melted inconel 718 and associated tensile properties. *JOM* **68**, 1012–1020 (2016).
207. Caiazzo F, Alfieri V, Corrado G, Argenio P. Laser powder-bed fusion of Inconel 718 to manufacture turbine blades. *Int J Adv Manuf Technol* **93**, 4023–4031 (2017).
208. Li SM, Xiao H, Liu KY, Xiao WJ, Li YQ et al. Melt-pool motion, temperature variation and dendritic morphology of Inconel 718 during pulsed- and continuous-wave laser additive manufacturing: a comparative study. *Mater Design* **119**, 351–360 (2017).
209. Du JH, Lu XD, Deng Q, Qu JL, Zhuang JY et al. High-temperature structure stability and mechanical properties of novel 718 superalloy. *Mater Sci Eng: A* **452–453**, 584–591 (2007).
210. Bean GE, Witkin DB, McLouth TD, Pate DN, Zaldivar RJ. Effect of laser focus shift on surface quality and density of Inconel 718 parts produced via selective laser melting. *Addit Manuf* **22**, 207–215 (2018).
211. Schneider J, Lund B, Fullen M. Effect of heat treatment variations on the mechanical properties of Inconel 718 selective laser melted specimens. *Addit Manuf* **21**, 248–254 (2018).
212. Georgilas K, Khan RHU, Kartal ME. The influence of pulsed laser powder bed fusion process parameters on Inconel 718 material properties. *Mater Sci Eng:A* **769**, 138527 (2020).
213. Popovich VA, Borisov EV, Popovich AA, Sufiiarov VS, Masaylo DV et al. Functionally graded Inconel 718 processed by additive manufacturing: crystallographic texture, anisotropy of microstructure and mechanical properties. *Mater Design* **114**, 441–449 (2017).
214. Smith DH, Bicknell J, Jorgensen L, Patterson BM, Cordes NL et al. Microstructure and mechanical behavior of direct metal laser sintered Inconel alloy 718. *Mater Characteriz* **113**, 1–9 (2016).
215. Chlebus E, Gruber K, Kuźnicka B, Kurzac J, Kurzynowski T. Effect of heat treatment on the microstructure and mechanical properties of Inconel 718 processed by selective laser melting. *Mater Sci Eng:A* **639**, 647–655 (2015).
216. Ni M, Chen C, Wang XJ, Wang PW, Li RD et al. Anisotropic tensile behavior of in situ precipitation strengthened Inconel 718 fabricated by additive manufacturing. *Mater Sci Eng:A* **701**, 344–351 (2017).
217. Valdez M, Kozuch C, Faierson EJ, Jasiuk I. Induced porosity in Super Alloy 718 through the laser additive manufacturing process: microstructure and mechanical properties. *J Alloys Compd* **725**, 757–764 (2017).
218. Wang ZM, Guan K, Gao M, Li XY, Chen XF et al. The microstructure and mechanical properties of deposited-IN718 by selective laser melting. *J Alloys Compd* **513**, 518–523 (2012).
219. Moussaoui K, Rubio W, Mousseigne M, Sultan T, Rezai F. Effects of Selective Laser Melting additive manufacturing parameters of Inconel 718 on porosity, microstructure and mechanical properties. *Mater Sci Eng:A* **735**, 182–190 (2018).
220. Lu YJ, Wu SQ, Gan YL, Huang TT, Yang CG et al. Study on the microstructure, mechanical property and residual stress of SLM Inconel-718 alloy manufactured by differing island scanning strategy. *Opt Laser Technol* **75**, 197–206 (2015).
221. Polmear I, StJohn D, Nie JF, Qian M. *Light Alloys: Metallurgy of the Light Metals* 5th ed (Elsevier, Boston, 2017).
222. Tradowsky U, White J, Ward RM, Read N, Reimers W et al. Selective laser melting of AlSi10Mg: influence of post-processing on the microstructural and tensile properties development. *Mater Design* **105**, 212–222 (2016).
223. Aboulkhair NT, Simonelli M, Parry L, Ashcroft I, Tuck C et al. 3D printing of Aluminium alloys: additive Manufacturing of Aluminium alloys using selective laser melting. *Prog Mater Sci* **106**, 100578 (2019).
224. Altıparmak SC, Yardley VA, Shi ZS, Lin JG. Challenges in additive manufacturing of high-strength aluminium alloys and current developments in hybrid additive manufacturing. *Int J Lightw Mater Manuf* **4**, 246–261 (2021).
225. Martin JH, Yahata BD, Hundley JM, Mayer JA, Schaedler TA et al. 3D printing of high-strength aluminium alloys. *Nature* **549**, 365–369 (2017).
226. Brandl E, Heckenberger U, Holzinger V, Buchbinder D. Additive manufactured AlSi10Mg samples using Selective Laser Melting (SLM): microstructure, high cycle fatigue, and fracture behavior. *Mater Design* **34**, 159–169 (2012).
227. Li W, Li S, Liu J, Zhang A, Zhou Y et al. Effect of heat treatment on AlSi10Mg alloy fabricated by selective laser melting: Microstructure evolution, mechanical properties and fracture mechanism. *Mater Sci Eng:A* **663**, 116–125 (2016).
228. Chen B, Moon SK, Yao X, Bi G, Shen J et al. Strength and strain hardening of a selective laser melted AlSi10Mg alloy. *Scr Mater* **141**, 45–49 (2017).
229. Awd M, Stern F, Kampmann A, Kotzem D, Tenkamp J et al. Microstructural characterization of the anisotropy and cyclic deformation behavior of selective laser melted AlSi10Mg structures. *Metals* **8**, 825 (2018).
230. Manfredi D, Calignano F, Krishnan M, Canali R, Ambrosio EP et al. From powders to dense metal parts: characterization of a commercial AlSiMg alloy processed through direct metal laser sintering. *Materials* **6**, 856–869 (2013).
231. Rosenthal I, Stern A, Frage N. Microstructure and mechanical properties of AlSi10Mg parts produced by the laser beam Additive Manufacturing (AM) technology. *Metallogr, Microstruct, Anal* **3**, 448–453 (2014).
232. Kempen K, Thijs L, Van Humbeeck J, Kruth JP. Processing AlSi10Mg by selective laser melting: parameter optimisation and material characterisation. *Mater Sci Technol* **31**, 917–923 (2015).
233. Anwar AB, Pham QC. Selective laser melting of AlSi10Mg: effects of scan direction, part placement and inert gas flow velocity on tensile strength. *J Mater Process Technol* **240**, 388–396 (2017).
234. Li X, Huang ZH, Qi WJ, Wang J, Li YJ et al. Microstructure and mechanical properties of AlSi10Mg alloy fabricated by SLM technology. *Mater Sci* **9**, 564–572 (2019).
235. Kempen K, Thijs L, Van Humbeeck J, Kruth JP. Mechanical properties of AlSi10Mg produced by selective laser melting. *Phys Proced* **39**, 439–446 (2012).
236. Fatemi A, Molaei R, Sharifimehr S, Phan N, Shamsaei N.

Multiaxial fatigue behavior of wrought and additive manufactured Ti-6Al-4V including surface finish effect. *Int J Fatigue* **100**, 347–366 (2017).

237. Shrestha R, Simsiriwong J, Shamsaei N, Thompson SM, Bian LK. Effect of build orientation on the fatigue behavior of stainless steel 316L manufactured via a laser-powder bed fusion process. In *27th Annual Solid Frefform Fabrication Symposium Proceedings* 605–616 (2016).
238. Raus AA, Wahab MS, Ibrahim M, Kamarudin K, Ahmed A et al. Mechanical and physical properties of AlSi10Mg processed through selective laser melting. *AIP Conf Proc* **1831**, 020027 (2017).
239. Shi J, Wang YC. Development of metal matrix composites by laser-assisted additive manufacturing technologies: a review. *J Mater Sci* **55**, 9883–9917 (2020).
240. Yadroitsev I, Bertrand P, Smurov I. Parametric analysis of the selective laser melting process. *Appl Surf Sci* **253**, 8064–8069 (2007).
241. Boley CD, Khairallah SA, Rubenchik AM. Calculation of laser absorption by metal powders in additive manufacturing. *Appl Opt* **54**, 2477–2482 (2015).
242. Irrinki H, Dexter M, Barmore B, Enneti R, Pasebani S et al. Effects of powder attributes and laser powder bed fusion (L-PBF) process conditions on the densification and mechanical properties of 17-4 PH stainless steel. *JOM* **68**, 860–868 (2016).
243. Heeling T, Cloots M, Wegener K. Melt pool simulation for the evaluation of process parameters in selective laser melting. *Addit Manuf* **14**, 116–125 (2017).
244. Bai YC, Yang YQ, Wang D, Zhang MK. Influence mechanism of parameters process and mechanical properties evolution mechanism of maraging steel 300 by selective laser melting. *Mater Sci Eng:A* **703**, 116–123 (2017).
245. Gu H, Wei C, Li L, Han QQ, Setchi R et al. Multi-physics modelling of molten pool development and track formation in multi-track, multi-layer and multi-material selective laser melting. *Int J Heat Mass Trans* **151**, 119458 (2020).
246. Yu GQ, Gu DD, Dai DH, Xia MJ, Ma CL et al. On the role of processing parameters in thermal behavior, surface morphology and accuracy during laser 3D printing of aluminum alloy. *J Phys D:Appl Phys* **49**, 135501 (2016).
247. Wang ZK, Yan WT, Liu WK, Liu MB. Powder-scale multi-physics modeling of multi-layer multi-track selective laser melting with sharp interface capturing method. *Comput Mech* **63**, 649–661 (2019).
248. Yan WT, Lian YP, Yu C, Kafka OL, Liu ZL et al. An integrated process –structure –property modeling framework for additive manufacturing. *Comput Methods Appl Mech Eng* **339**, 184–204 (2018).
249. Yang M, Wang L, Yan WT. Phase-field modeling of grain evolutions in additive manufacturing from nucleation, growth, to coarsening. *npj Comput Mater* **7**, 56 (2021).
250. Simonelli M, Tse YY, Tuck C. Effect of the build orientation on the mechanical properties and fracture modes of SLM Ti–6Al–4V. *Mater Sci Eng:A* **616**, 1–11 (2014).
251. Chen CP, Yin J, Zhu HH, Xiao ZX, Zhang L et al. Effect of overlap rate and pattern on residual stress in selective laser melting. *Int J Mach Tools Manu* **145**, 103433 (2019).
252. Chen CY, Xie YC, Yan XC, Yin S, Fukanuma H et al. Effect of hot isostatic pressing (HIP) on microstructure and mechanical properties of Ti6Al4V alloy fabricated by cold spray additive manufacturing. *Addit Manuf* **27**, 595–605 (2019).
253. Atkinson HV, Davies S. Fundamental aspects of hot isostatic pressing: an overview. *Metall Mater Trans A* **31**, 2981–3000 (2000).
254. Finfrock CB, Exil A, Carroll JD, Deibler L. Effect of hot isostatic pressing and powder feedstock on porosity, microstructure, and mechanical properties of selective laser melted AlSi10Mg. *Metallogr, Microstruct, Anal* **7**, 443–456 (2018).
255. Haan J, Asseln M, Zivcec M, Eschweiler J, Radermacher R et al. Effect of subsequent Hot Isostatic Pressing on mechanical properties of ASTM F75 alloy produced by Selective Laser Melting. *Powder Metal* **58**, 161–165 (2015).
256. Leuders S, Lieneke T, Lammers S, Tröster T, Niendorf T. On the fatigue properties of metals manufactured by selective laser melting — the role of ductility. *J Mater Res* **29**, 1911–1919 (2014).
257. Schneller W, Leitner M, Springer S, Grün F, Taschauer M. Effect of HIP treatment on microstructure and fatigue strength of selectively laser melted AlSi10Mg. *J Manuf Mater Process* **3**, 16 (2019).
258. Grzesik W. Hybrid additive and subtractive manufacturing processes and systems: a review. *J Mach Eng* **18**, 5–24 (2018).
259. Gibson I, Rosen D, Stucker B, Khorasani M. Hybrid additive manufacturing. Gibson I, Rosen D, Stucker B, Khorasani M, eds. *Additive Manufacturing Technologies*, 347–366 (Springer, Cham, 2021); https://doi.org/10.1007/978-3-030-56127-7_12.
260. Everton SK, Hirsch M, Stravroulakis P, Leach RK, Clare AT. Review of in-situ process monitoring and in-situ metrology for metal additive manufacturing. *Mater Design* **95**, 431–445 (2016).
261. Bisht M, Ray N, Verbist F, Coeck S. Correlation of *selective laser melting-melt pool* events with the tensile properties of Ti-6Al-4V ELI processed by laser powder bed fusion. *Addit Manuf* **22**, 302–306 (2018).
262. Tapia G, Elwany A. A review on process monitoring and control in metal-based additive manufacturing. *J Manuf Sci Eng* **136**, 060801 (2014).
263. Purtonen T, Kalliosaari A, Salminen A. Monitoring and adaptive control of laser processes. *Phys Proced* **56**, 1218–1231 (2014).
264. Furumoto T, Alkahari MR, Ueda T, Aziz MSA, Hosokawa A. Monitoring of laser consolidation process of metal powder with high speed video camera. *Phys Proced* **39**, 760–766 (2012).
265. Clijsters S, Craeghs T, Buls S, Kempen K, Kruth JP. In situ quality control of the selective laser melting process using a high-speed, real-time melt pool monitoring system. *Int J Adv Manuf Technol* **75**, 1089–1101 (2014).
266. Renken V, Von Freyberg A, Schünemann K, Pastors F, Fischer A. In-process closed-loop control for stabilising the melt pool temperature in selective laser melting. *Prog Addit Manuf* **4**, 411–421 (2019).
267. Wei KW, Lv M, Zeng XY, Xiao ZX, Huang G et al. Effect of laser remelting on deposition quality, residual stress, microstructure, and mechanical property of selective laser melting processed Ti-5Al-2.5Sn alloy. *Mater Characteriz* **150**, 67–77 (2019).
268. Chua CK, Wong CH, Yeong WY. *Standards, Quality Control, and Measurement Sciences in 3D Printing and Additive*

Manufacturing (Academic Press, London, 2017).

269. Mancisidor AM, Garciandia F, Sebastian MS, Álvarez P, Díaz J et al. Reduction of the residual porosity in parts manufactured by selective laser melting using skywriting and high focus offset strategies. *Phys Proced* **83**, 864–873 (2016).

Acknowledgements

The authors are grateful for the support of the National Key Research and Development Program of China [grant number 2018YFB1106301], Research and Development Program Project in Key Areas of Guangdong Province [grant number 2019B090907001 and 2019B010943001], Shenzhen Science and Technology Innovation Commission [grant number JCYJ20180504165824643], Natural Science Foundation of Guangdong Province [grant number 2020A1515011373], and the National Natural Science Foundation of China [grant number 51971108]. Dr. Ming Yan appreciates the support of the Humboldt Research Fellowship for Experienced Researchers.

Competing interests

The authors declare no competing financial interests.